Geochimica et Cosmochimica Acta 350 (2023) 1–15

Contents lists available at ScienceDirect

Geochimica et Cosmochimica Acta

journal homepage: www.elsevier.com/locate/gca

Thermally-induced clumped isotope resetting in belemnite and optical calcites: Towards material-specific kinetics

Nathan Looser [a,*], Paul Petschnig [a], Jordon D. Hemingway [a], Alvaro Fernandez [b], Luiz Morales Grafulha [a], Alberto Perez-Huerta [c], Madeleine L. Vickers [d], Gregory D. Price [e], Max W. Schmidt [a], Stefano M. Bernasconi [a]

[a] Department of Earth Sciences, ETH Zurich, Sonneggstrasse 5, CH-8092 Zurich, Switzerland
[b] Andalusian Institute of Earth Sciences, CSIC-University of Granada, Granada, Spain
[c] Department of Geological Sciences, The University of Alabama, Tuscaloosa, AL 35487, USA
[d] Centre for Earth Evolution and Dynamics (CEED), University of Oslo, P.O. Box 1028 Blindern, N-0315 Oslo, Norway
[e] School of Geography, Earth and Environmental Sciences, Plymouth University, Drake Circus, Plymouth PL4 8AA, UK

ARTICLE INFO

Associate editor: Weifu Guo

Keywords:
Carbonate clumped isotopes
Solid-state bond reordering
Mineral–water isotopic exchange
Belemnite rostral calcite
Optical calcite

ABSTRACT

The application of carbonate clumped isotope (Δ_{47}) thermometry in deep-time is often limited by modification of the original temperature signal by thermal resetting. New modeling approaches to estimate the initial isotopic composition of partially reset calcites and maximal burial temperatures, however, open promising avenues in temperature reconstruction. Such approaches strongly depend on laboratory-derived kinetic parameters of calcite materials, which may differ in their microstructure, water content and distribution, and minor and trace element composition, and thus may have different resetting kinetics. The rostra of belemnites, an extinct group of mollusks with a wide temporal and spatial occurrence in the Mesozoic, have been extensively used for deep-time paleoclimate reconstructions using oxygen isotope geochemistry. Belemnites are also important targets for clumped isotope-based temperature reconstructions, but often are found to have reset Δ_{47} compositions. Here, we present results from heating experiments on belemnite rostral calcite and optical calcite and provide belemnite-specific kinetic parameters for clumped isotope resetting. We show that belemnite calcite is altered faster and at lower temperatures than optical calcite and all other calcites reported in previous studies. We suggest that fast initial resetting results from oxygen isotope exchange of belemnite calcite with internal skeletal water present as fluid inclusions or organic-derived water, a process completed within 2–4 min at the experimental temperatures used here. Extrapolation to geological timescales using different solid-state bond reordering models shows that belemnite calcite resetting starts at lower burial temperatures than brachiopod, spar, and optical calcites. This susceptibility to thermal resetting results in a measurable (+3 °C) increase of the apparent Δ_{47} temperature even under shallow to moderate burial conditions (i.e., 40–50 °C for 10^6–10^7 years timescales). Following the overprint to higher apparent Δ_{47} temperatures during burial, the belemnite Δ_{47} may further re-equilibrate during exhumation resulting in a decrease of apparent Δ_{47} temperatures. Such "retrograde resetting" is similar to what is observed for carbonatites and marbles during cooling, and may cause underestimation of the thermal resetting a sample experienced during its geological history. Overall, our results demonstrate the importance of material-specific kinetic parameters and we urge caution when interpreting Δ_{47}-derived temperatures of biogenic carbonates from deep-time archives.

1. Introduction

Carbonate clumped isotope paleothermometry has been widely used for paleotemperature measurements related to climate and paleoenvironmental reconstructions (e.g., Came et al., 2007; Price et al., 2013; Vickers et al., 2020, 2021), diagenesis (e.g., Loyd et al., 2014; Millán et al., 2016), tectonic and burial histories (e.g., Huntington and Lechler, 2015; Looser et al., 2021), and metamorphism (e.g., Lloyd et al., 2017; Ryb et al., 2017; Brenner et al., 2021). The carbonate clumped isotope paleothermometer (expressed as Δ_{47}) is based on the increasing

* Corresponding author.
E-mail address: nathan.looser@erdw.ethz.ch (N. Looser).

https://doi.org/10.1016/j.gca.2023.03.030
Received 1 July 2022; Accepted 23 March 2023
Available online 29 March 2023

abundance of ^{13}C–^{18}O bonds in carbonate minerals, relative to a stochastic distribution, with decreasing temperatures (Wang et al., 2004; Ghosh et al., 2006; Schauble et al., 2006) and records the temperature during crystallization. The Δ_{47} paleothermometer is independent from the isotopic composition of the fluid from which the carbonate precipitates (Ghosh et al., 2006; Eiler, 2011), which is a major advantage compared to the traditional $\delta^{18}O$ paleothermometer.

A limitation of carbonate clumped isotope thermometry is the modification of the original temperature information during deep burial. In addition to recrystallization, the clumped isotope composition of a carbonate at elevated temperatures can be altered through diffusion-driven thermal resetting reactions that partially modify or even completely erase original temperature information (Passey and Henkes, 2012; Henkes et al., 2014; Stolper and Eiler, 2015). Thermal resetting takes place when carbonates experience temperatures high enough to overcome the activation-energy barrier for isotopic exchange and diffusion. In such cases, the measured Δ_{47} reflects an apparent temperature that ranges between the original crystallization temperature and the maximum temperature reached during burial. Diffusion-driven thermal resetting has traditionally been referred to as "solid state bond reordering" (Passey and Henkes, 2012; Henkes et al., 2014; Stolper and Eiler, 2015). This process involves the re-organization of ^{13}C and ^{18}O within the mineral lattice without interaction with an external medium. However, more recent work suggests that, at least for skeletal carbonates, resetting of Δ_{47} can also occur by isotopic exchange with internal water (this study, Staudigel and Swart, 2016; Nooitgedacht et al., 2021). We thus use the following nomenclature for thermally induced clumped isotope resetting in carbonates: "Solid-state bond reordering" for isotopic exchange between neighboring carbonate groups within the mineral lattice and "mineral–water isotopic exchange" for oxygen isotope exchange between carbonate molecules in the carbonate mineral lattice and water.

Thermal resetting may either increase or decrease apparent Δ_{47} temperatures. Specifically, the apparent Δ_{47} temperature increases if a sample initially crystallized at a low temperature is heated above the temperature at which resetting begins, but decreases if a sample initially crystallized at high temperatures is cooled below the temperature at which the apparent equilibrium is locked-in ("apparent equilibrium blocking temperature" Stolper and Eiler, 2015). Both scenarios have been observed in nature in: (1) pristine fossils with unrealistically high Δ_{47} temperatures without indications of recrystallization (e.g., Shenton et al., 2015; Fernandez et al., 2021); (2) sedimentary carbonates heated by magmatic intrusions (e.g., Lloyd et al., 2017; Brenner et al., 2021); and (3) carbonatites and marbles with lower Δ_{47} temperatures than igneous crystallization or peak metamorphic temperatures (e.g., Dennis and Schrag, 2010; Schmid and Bernasconi, 2010). Several factors are believed to control thermal resetting rates, with mineralogy being the most prominent. For instance, among aragonite, calcite, and dolomite, aragonite shows the fastest resetting and dolomite the slowest (Stolper and Eiler, 2015; Lloyd et al., 2017, 2018; Ritter et al., 2017; Ryb et al., 2017; Chen et al., 2019). Other factors discussed are the presence of water (Passey and Henkes, 2012; Staudigel and Swart, 2016; Brenner et al., 2018; Nooitgedacht et al., 2021), minor and trace element substitutions (Passey and Henkes, 2012; Henkes et al., 2014; Stolper and Eiler, 2015), and pressure (Passey and Henkes, 2012; Brenner et al., 2018).

Thermal resetting limits the utility of clumped isotopes to reconstruct paleoenvironmental conditions in deep-time as well as burial and tectonic histories of sedimentary basins. Nevertheless, approaches have been proposed to use partially reset carbonates to determine relative paleotemperature changes (Fernandez et al., 2021), reconstruct absolute temperatures of diagenetic cementation prior to heating during deep-burial (Lawson et al., 2018), and estimate peak burial temperatures in sedimentary basins (Henkes et al., 2014; Shenton et al., 2015; Ryb et al., 2021). Quantitative reconstructions, however, strongly depend on the choice of kinetic parameters for thermal resetting. Limitations of existing kinetic parameters relate to the fact that they have been derived for a limited set of materials that may differ in their microstructure, water content and distribution, and minor and trace element compositions from the samples of interest for a specific application. For calcite, data are available from two optical calcites (one heated under both wet and dry conditions), one spar, and one Permian brachiopod (Passey and Henkes, 2012; Henkes et al., 2014; Stolper and Eiler, 2015; Brenner et al., 2018). The absence of statistically significant differences in resetting kinetics between the studied optical and brachiopod calcites has been used as evidence for common kinetic parameters for all calcites (Henkes et al., 2014; Stolper and Eiler, 2015; Hemingway and Henkes, 2021), although relatively large uncertainties attributed to kinetic parameters may conceal possible differences. Other studies have argued that resetting kinetics indeed differ between optical and spar calcites (Passey and Henkes, 2012; Shenton et al., 2015; Stolper and Eiler, 2015); and different resetting rates between abiogenic and skeletal aragonite have been suggested by Staudigel and Swart (2016) and Chen et al. (2019) and confirmed by Nooitgedacht et al. (2021).

To date, three models with different mechanistic interpretations of solid-state bond reordering in calcites have been developed from laboratory heating experiments performed at different temperatures and timescales. A key finding in all heating experiments is that Δ_{47} change follows apparent non-first-order kinetics with a first rapid exponential decrease followed by a slower exponential decrease. The transient defect/equilibrium defect model (Passey and Henkes, 2012; Henkes et al., 2014) – here referred to as "He 14 model" – assumes that solid-state bond reordering is controlled by defects within the crystal lattice (e.g., point defects, dislocations, cation substitutions), some of which can be annealed by heating. Such defects promote diffusion of C and O through the crystal lattice and thus bond reordering. The rapid Δ_{47} decrease in the first stage of heating is attributed to the high initial abundance of lattice defects. With progressive heating, transient defects are annealed, resulting in a reduced mobility of C and O in the crystal lattice and, accordingly, slower solid-state bond reordering. Remaining unannealable equilibrium defects promote continued but slow C and O diffusion in the second stage of heating. This model implies that calcites with an initially high density of lattice defects should reorder faster than those with fewer defects. The paired exchange-diffusion model (Stolper and Eiler, 2015) – here referred to as "SE 15 model" – assumes that the initial rapid decrease in Δ_{47} occurs as doubly-substituted carbonate groups (containing ^{13}C and one ^{18}O) are removed by exchange with a neighboring group containing only ^{12}C and ^{16}O. This exchange results in the formation of two neighboring singly-substituted isotopologues, one containing the ^{13}C and the other the ^{18}O (together referred to as 'pairs'). As long as the two singly-substituted carbonate groups remain direct neighbors, they can immediately back-react to re-form a clump, thus buffering the decrease in Δ_{47}. In the second stage, the two carbonate groups that together comprise a pair slowly separate by diffusion through the crystal lattice such that each singly-substituted group (now referred to as a 'singleton') is surrounded by non-substituted neighbors, effectively halting back-reaction to a clump. Because singleton diffusion is slower than pair formation, pairs can accumulate. Back-reaction of these pairs to re-form clumps slows down the rate of Δ_{47} decrease until diffusion becomes the dominant mechanism. This reordering model implies that all calcites share a common reordering behavior, as there is no assumed influence of material-specific properties such as lattice defect concentration, crystal size, or texture. Different reordering rates between different mineralogies are explained by the crystal structure (Lloyd et al., 2018; Chen et al., 2019). The disordered kinetic model (Hemingway and Henkes, 2021) – here referred to as "HH 21 model" – is based on the concept that solid-state bond reordering rates arise naturally from random-walk ^{18}O diffusion through the crystal lattice. In contrast to the SE 15 and He 14 models, which assume a specific reordering mechanism, this model treats clumped isotope reordering as a disordered kinetic process whereby solid-state C–O isotope exchange occurs as a parallel superposition of first-order reactions.

In contrast to recrystallization, thermal resetting is not associated with petrographic, textural, or elemental changes (Passey and Henkes, 2012; Henkes et al., 2014; Shenton et al., 2015; Stolper and Eiler, 2015; Fernandez et al., 2021). Accordingly, excluding recrystallization of the calcite during heating is essential for interpreting the evolution of Δ_{47} as thermal resetting alone without modification by recrystallization processes. Changes in carbonate $\delta^{13}C$ and $\delta^{18}O$ may indicate open-system recrystallization or isotopic exchange with an external fluid or gas. However, a lack of change in $\delta^{13}C$ and $\delta^{18}O$ is insufficient to exclude recrystallization under closed-system conditions. We thus used electron backscatter diffraction (EBSD) to obtain high-resolution information at (sub)-μm scale on the orientation of the individual crystals of the belemnite samples, allowing to assess preservation of the primary textures (e.g., Pérez-Huerta et al., 2007, 2018) in the heated samples.

In this study, we compare the thermal resetting of belemnite rostral calcite with that of optical calcite. These two materials differ greatly in trace element substitution, crystal size, and distribution of internal water. Optical grade calcite is characterized by large crystals of high purity and its thermal resetting has been studied previously (Passey and Henkes, 2012; Stolper and Eiler, 2015; Brenner et al., 2018). Belemnites are fossil cephalopods, which are found in high abundance in Late Triassic to Late Cretaceous sediments in a broad range of paleoenvironments. Their internal shell, the so-called rostrum, is composed of low-Mg calcite, the most stable form of calcite with a high preservation potential (e.g., Stevens et al., 2017). Belemnite rostral calcite has been used extensively for paleoclimate reconstructions (e.g., Voigt et al., 2003; Mutterlose et al., 2010; Price et al., 2013; Bajnai et al., 2020; Fernandez et al., 2021; Vickers et al., 2021). Given the importance of belemnite calcite as deep-time paleoenvironmental archive, belemnite-specific kinetic parameters are desired to improve clumped isotope paleotemperature reconstructions.

2. Materials and methods

2.1. Optical calcite

The natural optical calcite used in our experiments originates from an unknown location in Mexico. The single crystal is transparent, devoid of macroscopic inclusions and impurities (Fig. S14a), and has a relatively high Δ_{47} value of 0.530 ± 0.009 ‰ (I-CDES, 95% CL), corresponding to a Δ_{47} temperature of 49 ± 4 °C, far from the equilibrium compositions at our experimental temperatures.

2.2. Belemnite rostral calcite

The belemnite rostrum studied here (*Cylindroteuthis*; Price et al., 2015) (Fig. S14b) originates from the Callovian (Middle Jurassic) Christian Malford Lagerstätte in the south-western UK and was presented in the study of Vickers et al. (2021). It has a Δ_{47} value of 0.610 ± 0.017 ‰ (I-CDES, 95% CL), corresponding to a Δ_{47} temperature of 20 ± 5 °C. The Christian Malford Lagerstätte is known for exceptional fossil preservation, including biogenic aragonite in ammonites and phragmocones of belemnites (Wilby et al., 2008; Price et al., 2015). Because the metastability of aragonite causes conversion to calcite under moderate temperatures (e.g., Marland, 1975), the preservation of such old biogenic aragonite is exceptional and requires very low burial temperatures. These are also indicated by low thermal maturity of organic matter, apatite fission track and vitrinite reflectance data, and stratigraphic constraints (Hudson and Martill, 1994; Green et al., 2001; Kenig et al., 2004; Glass et al., 2013). Moreover, Vickers et al. (2021) showed that the aragonitic phragmocones and calcitic rostra from the same belemnite specimens yield, within error, identical Δ_{47} temperatures between 20 and 30 °C. As aragonite is thermally reset at lower temperatures than calcite (Staudigel and Swart, 2016; Ritter et al., 2017; Chen et al., 2019), identical aragonite and calcite Δ_{47} temperatures strongly indicate that burial temperatures at Christian Malford never exceeded the temperature limit for aragonite Δ_{47} preservation and precludes any pre-heating and partial resetting of the belemnite rostral calcite.

2.3. Sample preparation and heating experiments

The optical calcite was cleaned with de-ionized water and ethanol, crushed in a ceramic mortar, and sieved, retaining the 250–1000 μm fraction. Pyrite covering the outer layer of the belemnite rostrum was removed with a hand-held drill at low speed to avoid heating of the calcite. Slices of 1–2 mm thickness were cut perpendicular to the axis of the rostrum with a diamond wire saw operated at low speed. The slices were further sub-divided into three to four pieces and the apical zone, which is commonly influenced by diagenesis (e.g., Li et al., 2013; Ullmann et al., 2015), was removed. Finally, they were cleaned with de-ionized water and ethanol. All samples were then dried at 70 °C for several hours to remove moisture, and stored in a desiccator.

Aliquots of 50–200 mg of belemnite rostrum and 200–500 mg of optical calcite were placed at the bottom of silica-glass tubes that were previously heated to 950 °C for ~12 h to remove contaminants. Between 16 and 67 mg of silver oxalate ($Ag_2C_2O_4$) was packed between two layers of silica-wool (Fig. 1), and the tube was then evacuated to 6.8 × 10^{-3} bar and sealed. Silver oxalate was added to produce a CO_2 atmosphere (e.g., Scheele and Hoefs, 1992) with a known isotope composition ($\delta^{13}C = -7.69 \pm 0.01$ ‰ (VPDB) and $\delta^{18}O = +1.20 \pm 0.09$ ‰ (VPDB)) to monitor open-system recrystallization/exchange and to stabilize the calcite during heating. The oxalate decomposition reaction $Ag_2C_2O_4 \rightarrow Ag_2 + 2CO_2$, which proceeds above ~140 °C, also provides elemental silver to efficiently remove sulfur compounds from the atmosphere. This minimizes the presence of SO ions in the source of the mass spectrometer that can cause isobaric interference on m/z 48, which is used as a monitor for contamination. For the belemnite, we additionally added silver wool to ensure complete removal of sulfur compounds (Fig. 1). All experiments were conducted in a Nabertherm box

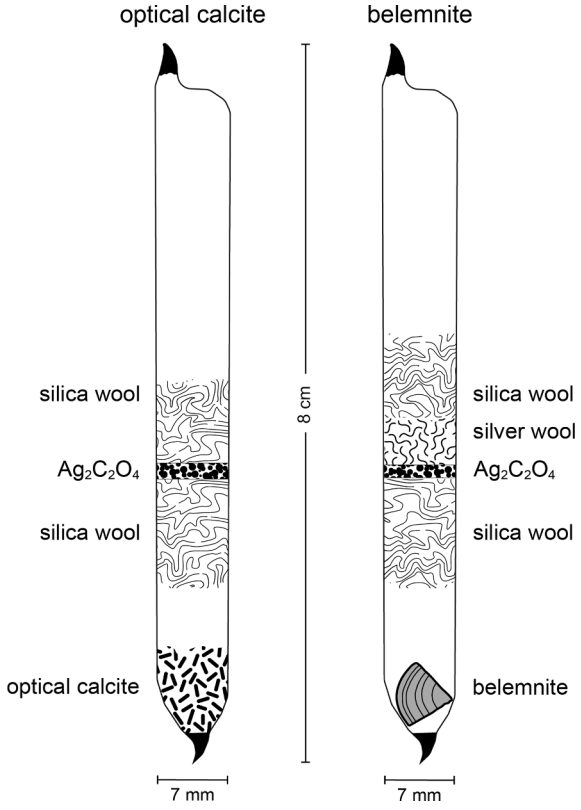

Fig. 1. Schematic diagram of the experimental setup.

furnace using a secondary K-type thermocouple directly adjacent to the samples at the center of the furnace to account for the offset between the built-in controlling thermocouple and true sample temperature. Experimental temperatures were held constant with an accuracy of ±2 °C for all temperatures, which ranged from 300 °C to 480 °C. Experiments were quenched to ~20 °C within seconds by dropping the glass tubes into a water bath.

2.4. Electron backscatter diffraction (EBSD)

For EBSD analysis, sample pieces were mounted in epoxy and mechanically polished to 0.25 μm diamond solution grain size, followed by chemical–mechanical polishing with an alkaline solution of colloidal silica in a neoprene substrate. Analyses were performed on coated samples (~2.5 nm carbon) in a Thermo Fisher - FEI Quanta 200F equipped with an EDAX Hikari EBSD camera using TEAM software for data acquisition at the Scientific Center for Optical and Electron Microscopy (ScopeM) at ETH Zurich. Acquisition parameters included accelerating voltage of 20 kV, beam current of 8 nA, working distance of 17 mm, and mapping step size of 1 μm. Post-acquisition processing included grain confidence index (CI) standardization followed by one step of grain CI correlation. All points with CI < 0.1 and grains with less than 10 pixels were removed to prevent artifacts. EBSD data are presented as crystallographic orientation maps and stereographic projections (pole figures) in relation to the (0001) and (10–14) planes of calcite.

2.5. Clumped isotope geochemistry

For clumped isotope analyses, samples were ground with a ceramic mortar and pestle. All measurements were conducted at ETH Zurich using a Thermo Scientific Kiel IV carbonate device coupled to a Thermo Scientific MAT253 isotope ratio mass spectrometer (IRMS) based on the methods described by Meckler et al. (2014), Müller et al. (2017), and Bernasconi et al. (2018). Potential isobaric contaminants on m/z 47 were removed by a Porapak Q trap held at −40 °C and monitored according to Davies and John (2017). Backgrounds on m/z 44–47 were determined at the beginning of each analytical session by high-voltage peak scans at five different intensities between 10 and 30 V (Bernasconi et al., 2013). Data reduction was carried out with the Easotope software package (John and Bowen, 2016). A total of 28 samples of optical calcite and 56 samples of belemnite rostrum were analyzed at least 10 times each. From a total of 990 measurements, 25 (~2.5%) were removed as outliers (see Appendix). Uncertainties in Δ_{47} are reported with margins of error at the 95% confidence level (Fernandez et al., 2017). Carbon and oxygen isotope ratios are reported relative to VPDB and are within analytical uncertainty of ±0.10 ‰ for $\delta^{13}C$ and ±0.20 ‰ for $\delta^{18}O$ (±1 std. dev). Clumped isotope data are reported in the I-CDES scale (Bernasconi et al., 2021), and Δ_{47} temperatures and equilibrium compositions are calculated using the Anderson et al. (2021) calibration.

2.6. Minor and trace element analyses

Minor and trace element ratios (Mg/Ca, Mn/Ca, Fe/Ca, and Sr/Ca) were analyzed on an Agilent 8800 Triple Quadrupole ICP-MS at ETH Zurich. Normalization and drift correction was applied using in-house standards.

2.7. Modeling

Kinetic parameters for all experiments using the He 14, SE 15, and HH 21 models were determined using the "Isotopylog" Python package (Hemingway, 2020). Optimal rate constants and their uncertainty for each experiment were calculated using an error-weighted fit to all data points. For the HH 21 model, regularized inverse solutions were first calculated and determined to be approximately lognormal (Figs. S8 and S9). Lognormal distributions were used for the determination of underlying activation energy parameters using an Arrhenian approach (Fig. S12). The optical calcite experiments run at 300 and 360 °C yielded a signal-to-noise ratio <3 (Figs. 2 and S9a, S10e, S11e) and were thus omitted from further analysis in accordance with previously defined signal-to-noise thresholds (Hemingway and Henkes, 2021). All SE 15 model results were determined with an initial pair slope dependence of $m_p = 0.0992$, as this is the value originally reported in Stolper and Eiler (2015) and used in all subsequent studies (e.g., Lloyd et al., 2018; Chen et al., 2019).

Because this practice led to the retention of only two optical calcite experiments of our study, which is insufficient to determine Arrhenius regression uncertainty, we did not calculate activation energies for this material but instead used previously published optical calcite values (Passey and Henkes, 2012; Passey et al., 2014; Stolper and Eiler, 2015; Hemingway and Henkes, 2021). In contrast, belemnite experiments at all temperatures yielded signal-to-noise ratios >10, allowing us to determine activation energy parameters. The Δ_{47} resetting over geologic timescales was determined in Isotopylog following the method of Hemingway and Henkes (2021).

3. Results

3.1. Stable isotopes and clumped isotopes

3.1.1. Optical calcite

The $\delta^{13}C$, $\delta^{18}O$, and Δ_{47} of all experiments are presented in Fig. 2 and Table S1. The unheated optical calcite has an initial $\Delta_{47} = 0.530 \pm 0.009$ ‰ (I-CDES, 95% CL) corresponding to 49 ± 2 °C, a $\delta^{13}C = -12.01$ ‰ (VPDB), and a $\delta^{18}O = -13.96$ ‰ (VPDB). The $\delta^{13}C$ and $\delta^{18}O$ for all heated samples are constant within ±0.05 ‰ of the unheated material while the Δ_{47} decreased with increasing heating time and temperature. The rate of change in Δ_{47} increased with increasing temperature but the expected equilibrium Δ_{47} at the experimental temperatures were never reached. The change in Δ_{47} compared to the unheated material ($\Delta\Delta_{47}$) after 96 h of heating was −0.008 ‰ for 300 °C, −0.038 ‰ for 360 °C, −0.162 ‰ for 420 °C, and −0.222 ‰ for 480 °C experiments.

3.1.2. Belemnite rostral calcite

The $\delta^{13}C$, $\delta^{18}O$, and Δ_{47} of all experiments are shown in Fig. 3 and in Table S2. The initial Δ_{47} of unheated belemnite is 0.610 ± 0.017 ‰. This value is confirmed by a second sample yielding 0.605 ± 0.016 ‰ that was analyzed to assess Δ_{47} variability of different regions in the rostrum, as individual pieces – rather than homogenized sample material – were used for these experiments. Similar to the optical calcite, Δ_{47} values in all experiments decreased with longer heating, and the rate of change in Δ_{47} increased with higher temperatures. The $\Delta\Delta_{47}$ compared to the unheated material after 96 h of heating was −0.178 ‰ at 300 °C, −0.255 ‰ at 360 °C, −0.362 ‰ at 420 °C, and −0.402 ‰ at 480 °C. Belemnite calcite reached Δ_{47} values within error of the equilibrium compositions after heating for 96 h at 420 °C and 2 h at 480 °C.

The $\delta^{13}C$ and $\delta^{18}O$ of 20 unheated samples, drilled from different areas of the rostrum, yielded values from +2.03 to +2.92 ‰ and −0.99 to −0.31 ‰, respectively. Compared to the values measured on the specific slice of rostral calcite used to determine initial Δ_{47} ($\delta^{13}C = +2.34$ ‰, $\delta^{18}O = -0.53$ ‰), this corresponds to a range between −0.31 and +0.58 ‰ for $\delta^{13}C$ and between −0.46 and +0.22 ‰ for $\delta^{18}O$ (Fig. 3), which we take to represent natural variability within the rostrum. Accordingly, observed $\delta^{13}C$ values for all heated samples are within natural variability. However, $\delta^{18}O$ values of heated samples are on average 0.4 ‰ lower than those of the unheated belemnite. This change in $\delta^{18}O$ occurs within the first 2–4 min of heating, coeval with a drop in Δ_{47} of −0.057 ‰ at 360 °C, −0.169 ‰ at 420 °C, and −0.244 ‰ at 480 °C. The $\delta^{18}O$ remains unchanged afterwards, and the Δ_{47} further decreases at lower rates (Fig. 3, Fig. S5d, and Table S2).

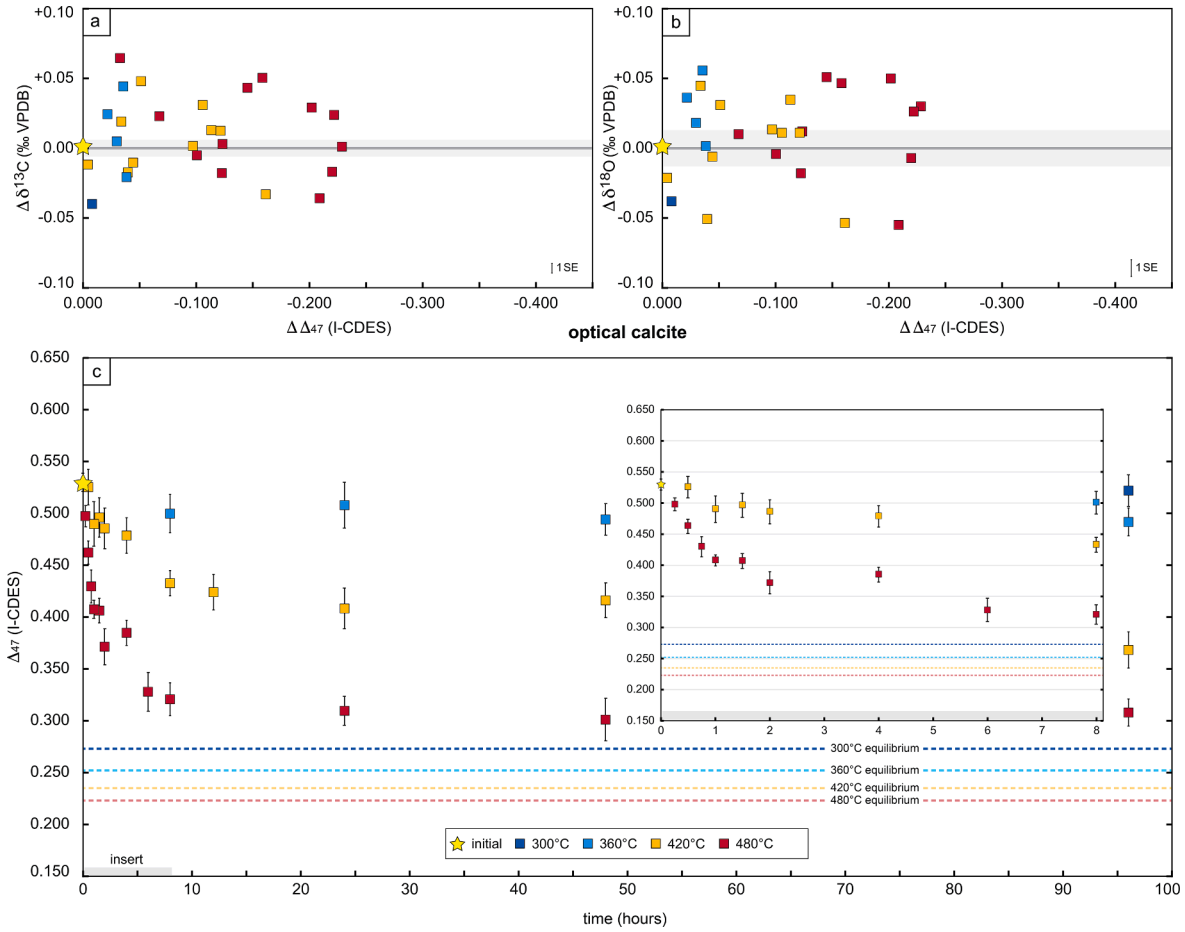

Fig. 2. Results for optical calcite heating experiments. 2a and 2b: Change in $\delta^{13}C$ ($\Delta\delta^{13}C$) and $\delta^{18}O$ ($\Delta\delta^{18}O$) plotted against the change in Δ_{47}, all relative to unheated sample material. The analytical uncertainty on $\delta^{13}C$ and $\delta^{18}O$ for individual samples is ±0.01 ‰ (1 SE). No obvious trends are observed for either $\Delta\delta^{13}C$ or $\Delta\delta^{18}O$. 2c: Clumped isotope evolution of optical calcite for each heating experiment. Dark blue represents 300 °C, light blue 360 °C, orange 420 °C, and red 480 °C experimental temperatures. The yellow star indicates unheated material. Uncertainty in Δ_{47} (I-CDES) values are given as 95% confidence intervals, and equilibrium values are determined following Anderson et al. (2021). The inset shows the first 8 h of Δ_{47} evolution in detail.

3.2. EBSD

Samples heated at 360 °C, 420 °C, and 480 °C for up to 96 h show the same arrangement of calcite crystals as the unheated belemnite, with growth from the rostrum center (nucleation point) towards the outer surface forming elongated pseudo-prismatic or columnar crystals (Fig. 4). The crystals show an overall orientation of the calcite *c*-axis perpendicular to the outer surface and a similar orientation in reference to the calcite cleavage plane (10–14).

3.3. Minor and trace element measurements

Optical and belemnite calcites Mg/Ca, Mn/Ca, Sr/ Ca, and Fe/Ca ratios are presented in Table S3. Belemnite calcite shows a 32 times higher total concentration of calcium substitutions ((Mg + Mn + Sr + Fe)/Ca) compared to the optical calcite. In the belemnite calcite, Mg and Sr are the most abundant calcium substituting cations with similar concentrations, while the concentrations of Mn and Fe are 400 and 1300 times lower (Table S3). In the optical calcite, Mg and Mn are the most common cations and Fe and Sr occur in by factors of 6 and 15 lower concentrations.

4. Discussion

4.1. Assessment of mineral preservation during heating

4.1.1. Stable isotope composition

Constant $\delta^{13}C$ and $\delta^{18}O$ has been observed for all abiogenic calcites and aragonites heated under dry conditions (this study, Passey and Henkes, 2012; Stolper and Eiler, 2015; Chen et al., 2019), even when heated in a CO_2 atmosphere with isotopic compositions very different from the carbonate. Thus, bulk isotope data of abiogenic calcite indicate no open-system recrystallization or substantial isotopic exchange with the CO_2 atmosphere during heating. In contrast, the decrease in $\delta^{18}O$ observed for belemnite calcite indicates loss or gain of oxygen isotopically distinct from the initial carbonate. X-ray diffraction analysis of unheated and heated samples show that this change is not related to phase transformation (Fig. S7). The CO_2 atmosphere used here has a similar $\delta^{18}O$ and a ~10 ‰ lower $\delta^{13}C$ than the belemnite calcite; substantial isotopic exchange should thus shift the belemnite $\delta^{13}C$ to lower values, whereas the constant $\delta^{13}C$ indicate no significant isotopic exchange between calcite and CO_2 and/or intra-crystalline organic matter. Control experiments conducted without addition of silver oxalate show similar shifts in $\delta^{18}O$ and Δ_{47} and thus speak against any influence of the silver oxalate on stable and clumped isotope compositions (Table S4).

A decrease in $\delta^{18}O$ of similar magnitude has also been observed for: (1) brachiopod calcite, which shifted by −0.2 to −0.4 ‰ for heating in a dry CO_2 atmosphere (Henkes et al., 2014); (2) biogenic aragonites

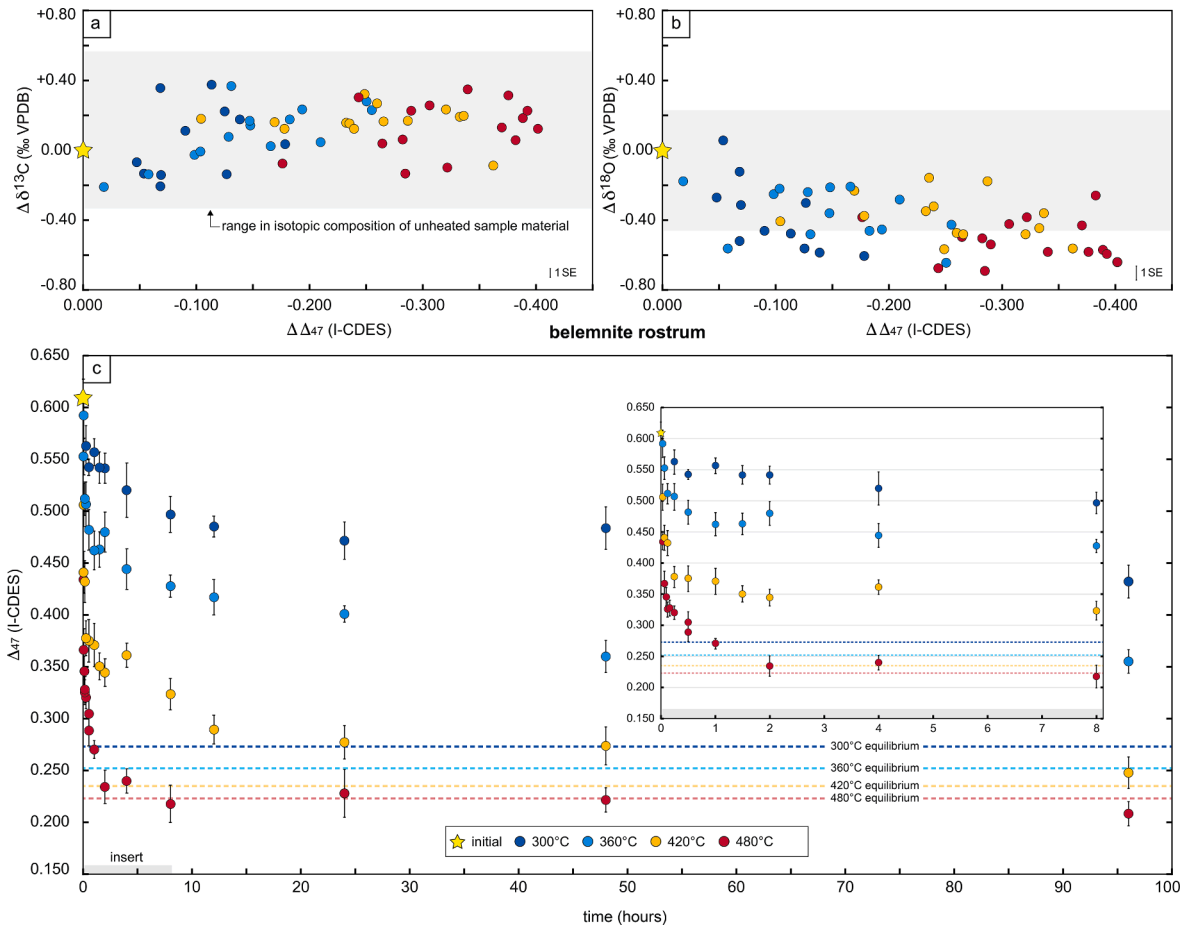

Fig. 3. Results for belemnite rostral calcite heating experiments. 3a and 3b: Change in $\delta^{13}C$ ($\Delta\delta^{13}C$) and $\delta^{18}O$ ($\Delta\delta^{18}O$) plotted against the change in Δ_{47}, relative to the unheated sample material. The analytical uncertainty on $\delta^{13}C$ and $\delta^{18}O$ for individual samples is ±0.01 ‰ (1 SE). While $\Delta\delta^{13}C$ is consistently within natural variability (gray shaded region), $\Delta\delta^{18}O$ reaches on average 0.4 ‰ lower values that cannot be explained by natural variability. 3c: Clumped isotope evolution of belemnite rostral calcite for each heating experiment. Dark blue represents 300 °C, light blue 360 °C, orange 420 °C, and red 480 °C experimental temperatures. The yellow star indicates unheated material. Uncertainty in Δ_{47} (I-CDES) values are given as 95% confidence intervals, and equilibrium values are determined following Anderson et al. (2021). The inset shows the first 8 h of Δ_{47} evolution in detail.

heated in a dry CO_2 atmosphere, in air, and under vacuum (Staudigel and Swart, 2016; Nooitgedacht et al., 2021), which shifted by up to −0.5 ‰ prior to conversion to calcite; and (3) optical and spar calcites heated in water under high-pressure, which led to $\delta^{18}O$ shifts of up to −0.6 ‰ (Passey and Henkes, 2012; Brenner et al., 2018). In all cases, $\delta^{13}C$ remained unchanged. Henkes et al. (2014) observed a condensed fluid in the tubes after heating of brachiopod calcite and hypothesized that it originated from decrepitation of fluid inclusions and/or hydrolysis of organic matter occluded in the shell. Staudigel and Swart (2016) suggested that the decrease in $\delta^{18}O$ of biogenic aragonite during heating was caused by equilibration with internal skeletal water. This was subsequently demonstrated by Nooitgedacht et al. (2021) by comparing the isotope compositions of aragonite and internal skeletal water before and after heating. The available evidence thus suggests that oxygen isotope exchange between the mineral and water – rather than CO_2 – causes the observed $\delta^{18}O$ decreases. In fact, a change in $\delta^{18}O$ occurred only in experiments where water was present, either as internal skeletal water or when added to the experiments. In contrast, $\delta^{18}O$ remained constant in all water-free experiments.

The amount of internal water needed to explain the observed belemnite $\delta^{18}O$ shift can be estimated by the following mass balance:

$$O_{water}(at\%\ of\ total\ oxygen) = \left(1 - \frac{\delta^{18}O_{calcite,\ heated} - \delta^{18}O_{water,\ initial}}{\delta^{18}O_{calcite,\ initial} - \delta^{18}O_{water,\ initial}}\right) \times 100$$

Assuming an internal water reservoir with a seawater-like initial $\delta^{18}O$ of −1 to +1 ‰ (V-SMOW) that fully exchanges with the calcite, and neglecting water-calcite fractionation at the experimental temperatures for simplicity, we find that the observed 0.4 ‰ shift in the calcite can be explained if 1.0–1.6 at% of the total oxygen reservoir in belemnite calcite is present from internal water. This corresponds to up to ~0.5–0.9 wt% internal water, in agreement with estimates of up to 3 wt % in modern skeletal carbonates (Gaffey, 1988). However, although the stable isotope compositions do not suggest that belemnite calcite was subjected to open-system recrystallization during the heating, textural constraints on the preservation state are required to further preclude the possibility of closed-system recrystallization.

4.1.2. *Belemnite micro-structure*

The micro-structure of belemnite rostra of several species is well-known (e.g., Stevens et al., 2017; Vickers et al., 2020; Hoffmann and Stevens, 2020, and references therein). EBSD imaging of the rostrum of the species *Neohibolites minimus*, as in other species, shows columnar calcite crystals radiating from the center with the *c*-axis perpendicular to the outer surface (Stevens et al., 2017). Our unheated belemnite shows this typical rostrum micro-structure (Fig. 4) without secondary mineral phases and/or recrystallization due to diagenesis. This micro-structure is also completely preserved in the heated samples, confirming that no recrystallization occurred during heating. Therefore, we conclude that the kinetic parameters derived in this study represent pristine belemnite rostral calcite and that all observed changes in Δ_{47} can be ascribed to

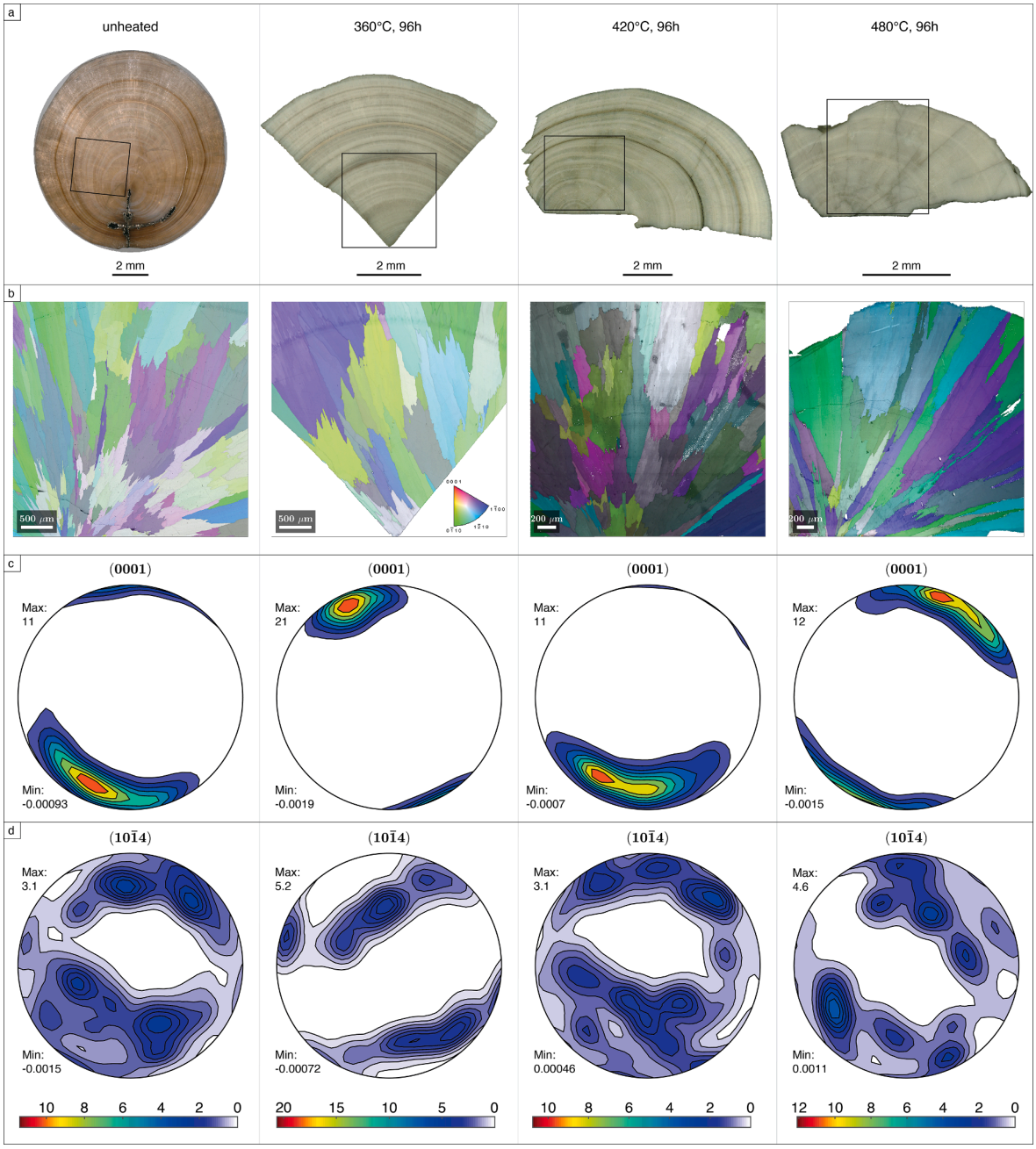

Fig. 4. Images and electron backscatter diffraction (EBSD) data of the belemnite rostrum used in our experiments. 4a: Cross-sections of the unheated (left) and heated at 360 °C, 420 °C, and 480 °C for 96 h rostrum pieces. Note the change in color between unheated (brown) and heated (grey) samples, which we ascribe to decomposition of organic components during heating. Black squares show the location and orientation of the EBSD maps b-d. 4b: Crystallographic orientation map with inverse pole figure (IPF) color-coding on top of the image quality (IQ) map with brighter areas diffracting more and thus yielding better quality of the diffraction pattern. 4c: Stereographic projections in relation to the (0001) plane of calcite. 4d: Stereographic projections in relation to the (10–14) plane of calcite. Cross-section image and EBSD crystallographic orientation map of the unheated belemnite are from Vickers et al. (2021).

thermal resetting.

4.2. Solid-state bond reordering in optical calcites and belemnites

4.2.1. Reaction progress during heating

In all our experiments, belemnite calcite shows a faster reaction progress than optical calcite, including an abrupt decrease in Δ_{47} within the first 2–4 min of heating and a larger total decrease in Δ_{47}. When heated at 300 °C, the optical calcite retained its initial Δ_{47} throughout the experiment, whereas the belemnite decreased by 0.178 ‰. At 480 °C, the belemnite shows a Δ_{47} near equilibrium after only 2 h, whereas optical calcite still remained 0.085 ‰ above equilibrium after 96 h.

Because our clumped isotope data are reported in the I-CDES scale, they can be directly compared to those of previous studies recalculated to the CDES scale at 90 °C by Hemingway and Henkes (2021) (Fig. 5). Our optical calcite shows a very similar reaction progress to that of the optical calcite in Stolper and Eiler (2015) and of the spar calcite in Passey and Henkes (2012), but a slower decrease than the optical calcite of Passey and Henkes (2012). Compared to all optical and spar calcites as well as the brachiopod calcite of Henkes et al. (2014), our belemnite calcite consistently shows the fastest reaction progress and is the only calcite material tested to date that approaches equilibrium at 420–430

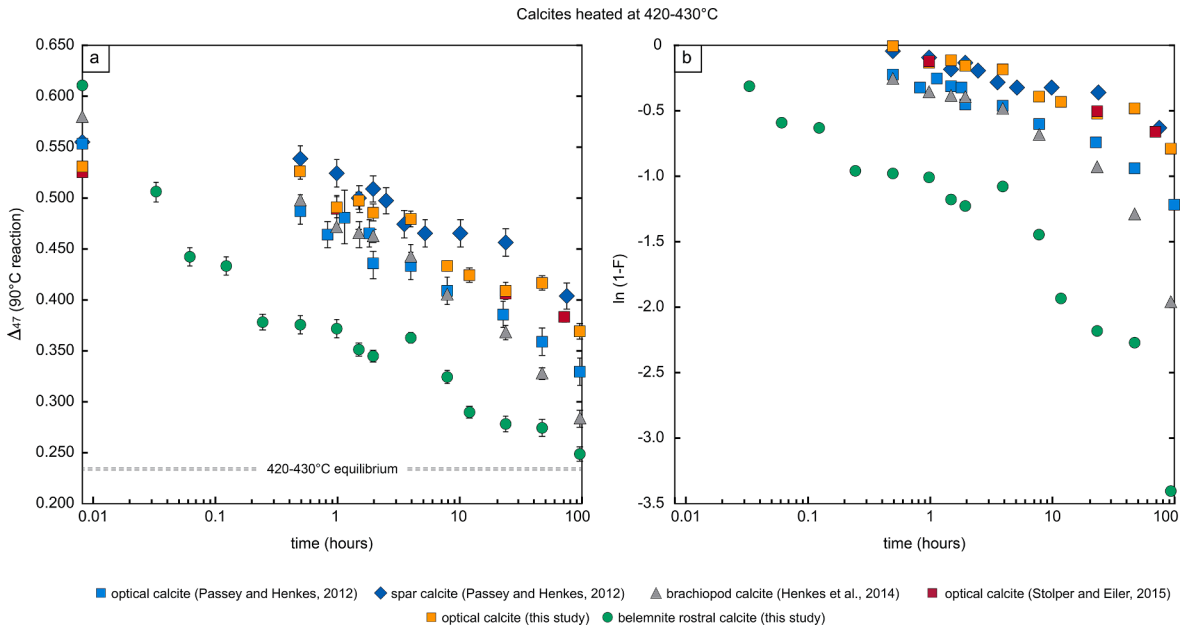

Fig. 5. 5a: Comparison of absolute Δ_{47} composition evolution of different calcites heated at 420–430 °C. Uncertainty in Δ_{47} (I-CDES or CDES at 90 °C) values are given as ±1 SE to compare with published values. Equilibrium values are determined following Anderson et al. (2021). 5b: Comparison of reaction progress of different calcites heated at 420–430 °C plotted as ln (1-F), with the reaction progress variable F defined as: $F = (\Delta_{47,\ init} - \Delta_{47,\ t}) / (\Delta_{47,\ init} - \Delta_{47\ equil})$.

°C within the first 100 h of heating.

4.2.2. Kinetic parameters

Belemnite Arrhenius parameters determined for the HH 21, SE 15, and He 14 models obtained from fitting our experimental data are presented in Table 1. For the HH 21 model, the calculated belemnite mean activation energy is $\mu_E = 167.7 \pm 12.3$ kJ mol^{-1} (±1 std. dev.), significantly lower than for all other calcites, which have $\mu_E = 247.4 \pm 15.6$ to 290.2 ± 27.1 kJ mol^{-1} (Hemingway and Henkes, 2021). Furthermore, the belemnite Arrhenius pre-exponential factor is calculated to $\nu_0 = 25.6 \pm 2.2$ min^{-1}, also significantly lower than for all other calcites, which yield $\nu_0 = 34.2 \pm 2.3$ to 42.7 ± 4.6 min^{-1}(Hemingway and Henkes, 2021). Lower mean activation energy and pre-exponential factor result from faster Δ_{47} reordering rates (Fig. 5). Interestingly, however, the calculated belemnite activation energy distribution width is $\sigma_E = 21.6 \pm 2.8$ kJ mol^{-1}, similar to other calcites, which range from $\sigma_E = 13.5 \pm 2.7$ to 24.3 ± 0.8 kJ mol^{-1} (Hemingway and Henkes, 2021). Although the exact reordering mechanism is not yet confirmed, a similar σ_E between all calcite materials despite differing μ_E and ν_0 values supports the idea proposed in Hemingway and Henkes (2021) that the activation energy distribution width reflects the range of O–O distances between neighboring carbonate groups, which is intrinsic to a given mineral crystal lattice.

For the SE 15 model, the activation energy for the belemnite "forward pair reaction" determined here ($E_f = 131.2 \pm 12.6$ kJ mol^{-1}) is significantly lower than for the optical calcite from Mexico ($E_f = 172.1 \pm 5.0$ kJ mol^{-1}; Stolper and Eiler, 2015). However, similar to σ_E in the HH 21 model, the calculated belemnite "diffusion of singleton" activation energy ($E_{ds} = 194.3 \pm 4.2$ kJ mol^{-1}) and both Arrhenius pre-exponential factors ($\ln(k_{0,f}) = 22.8 \pm 2.5$ min^{-1}; $\ln(k_{0,ds}) = 30.4 \pm 0.8$ min^{-1}) are statistically identical to those of optical calcite ($E_{ds} = 211.2 \pm 30.8$ kJ mol^{-1}, $\ln(k_{0,f}) = 25.2 \pm 0.7$ min^{-1}; $\ln(k_{0,ds}) = 28.9 \pm 4.5$ min^{-1}; Stolper and Eiler, 2015). Following the SE 15 model interpretation, this would suggest that belemnite clumps dissociate to form pairs (and vice versa) more quickly than in optical calcite, but that singleton diffusion through the crystal lattice proceeds at similar rates in both materials.

Finally, for the He 14 model, the calculated activation energies for belemnite equilibrium defect reordering and transient defect reordering are $E_c = 113.9 \pm 27.9$ kJ mol^{-1} and $E_d = 83.1 \pm 7.7$ kJ mol^{-1}, respectively. This is significantly lower than for optical and brachiopod calcite ($E_c = 187.6 \pm 2.7$ to 196.6 ± 19.1 kJ mol^{-1} and $E_d = 133.3 \pm 11.9$ to 180.0 ± 5.7 kJ mol^{-1}; Henkes et al., 2014). Arrhenius pre-exponential factors are similarly lower, with belemnite $\ln(k_{0,c}) = 13.0 \pm 5.0$ min^{-1} and $\ln(k_{0,d}) = 12.4 \pm 1.3$ min^{-1} (previous values: $\ln(k_{0,c}) = 24.0$ to 25.2 min^{-1} and $\ln(k_{0,d}) = 17.1$ to 25.5 min^{-1}; Henkes et al., 2014). Interestingly, the activation energy and Arrhenius pre-exponential factor controlling the rate at which transient defects are annealed in belemnite are $E_2 = 57.1 \pm 6.7$ kJ mol^{-1} and $\ln(k_{0,2}) = 8.0 \pm 1.1$ min^{-1}, respectively. These are within the range of values for brachiopod ($E_2 = 136.1 \pm 3.7$ kJ mol^{-1} and $\ln(k_{0,2}) = 18.5$ min^{-1}) and optical calcite ($E_2 = 47.9 \pm 21.2$ kJ mol^{-1} and $\ln(k_{0,2}) = 3.0$ min^{-1}; Henkes et al., 2014). Within the He 14 model framework, this would imply that belemnite defects – both equilibrium and transient – lead to faster Δ_{47} reordering than in previously analyzed materials, but that the rate of transient defect annealing is insensitive to material-specific differences.

Table 1
Belemnite Arrhenius parameters calculated for all existing models using the data presented in this study (n = 4). Parameter nomenclature follows that of the original publications, where E is activation energy and ν_0 or k_o is the pre-exponential factor (Henkes et al., 2014; Stolper and Eiler, 2015; Hemingway and Henkes, 2021). All uncertainty is ± 1 std. dev.; ds = "dif-single".

Model	Arrhenius parameters					
HH 21	μ_E kJmol^{-1}	ν_0 min^{-1}	σ_E kJmol^{-1}			
	167.7 ± 12.3	25.6 ± 2.2	21.6 ± 2.8			
SE 15	E_f kJmol^{-1}	$\ln(k_{0,f})$ min^{-1}	E_{ds} kJmol^{-1}	$\ln(k_{0,ds})$ min^{-1}		
	131.2 ± 12.6	22.8 ± 2.5	194.3 ± 4.2	30.4 ± 0.8		
He 14	E_c kJmol^{-1}	$\ln(k_{0,c})$ min^{-1}	E_d kJmol^{-1}	$\ln(k_{0,d})$ min^{-1}	E_2 kJmol^{-1}	$\ln(k_{0,2})$ min^{-1}
	113.9 ± 27.9	13.0 ± 5.0	83.1 ± 7.7	12.4 ± 1.3	57.1 ± 6.7	8.0 ± 1.1

4.3. The effect of water on clumped isotope resetting

In calcites, oxygen self-diffusion under wet conditions in the temperature range of our experiments is at least three orders of magnitude faster than under dry conditions because of rapid oxygen isotope exchange between the carbonate mineral and water at the crystal-water interface (Kronenberg et al., 1984; Farver, 1994; Labotka et al., 2011). Oxygen isotope exchange with water, resulting in a decrease of carbonate $\delta^{18}O$, has been observed in numerous heating experiments, either when water is added to the experiments (i.e., optical and spar calcites; Passey and Henkes, 2012; Brenner et al., 2018) or is present as internal water in biogenic calcites and aragonites (this study, Henkes et al., 2014; Staudigel and Swart, 2016; Nooitgedacht et al., 2021).

Regarding the influence of isotopic exchange between the mineral lattice and water on clumped isotope resetting, the previous experiments show contrasting effects: heating of optical calcite under wet, low-pressure conditions and of spar calcite under wet, high-pressure (100 MPa) conditions did not show differences in reaction progress compared to corresponding dry experiments (Passey and Henkes 2012). Similarly, Brenner et al. (2018) reported only a modest increase in resetting rates for optical calcite under wet, high-pressure (100 MPa) compared to dry, low-pressure conditions (higher pre-exponential factors but statistically identical activation energies). Finally, the brachiopod calcite experiments of Henkes et al. (2014) conducted under dry, low-pressure conditions show evidence for oxygen isotope exchange with internal water, as $\delta^{18}O$ decreased during heating and those authors observed the presence of a condensed fluid within sample tubes after quenching. However, this brachiopod calcite did not show significantly different resetting kinetics compared to abiogenic calcites. In contrast, considerably faster reaction progress for biogenic aragonite containing internal water compared to abiogenic aragonite with no or little internal water has been demonstrated in the experiments of Chen et al. (2019), Staudigel and Swart (2016), and Nooitgedacht et al. (2021).

The contrasting findings for abiogenic and skeletal carbonates can be explained by the efficiency of oxygen isotope exchange between the total crystal volume and water. Tracer diffusion studies show that at laboratory timescales, oxygen isotope diffusion into calcite is limited to short distances of less than 2 μm (Farver, 1994; Labotka et al., 2011). Therefore, for a given crystal volume, a larger surface area of the crystal-water interface causes a greater effect of the oxygen isotope exchange on the total crystal. The ratio between the surface area of the crystal-water interface and the total volume of crystal (S/V-ratio) is a material-specific property that depends on crystal size and geometry as well as water content and distribution. Abiogenic carbonates are typically composed of relatively large individual crystals and contain internal water in the form of fluid inclusions and thus exhibit small S/V ratios. In contrast, skeletal carbonates have complex micrometer-scale morphologies with individual crystals surrounded by inter-crystalline organic matrix and are composed of nanometer-size granules (Dauphin et al., 2018; Pérez-Huerta et al., 2018; Cuif et al., 2020). The carbonate nanogranules are surrounded by an intra-crystalline amorphous-organic phase that contains internal water (Gaffey, 1988). Preservation of intra-crystalline amorphous-organic phases has been shown in fossil corals as old as Devonian in age (Pérez-Huerta et al., 2018). In skeletal carbonates, internal water is thus present as fluid inclusions and associated with inter- and intra-crystalline organic matter within the biomineral (Gaffey, 1988; Cuif et al., 2004). In particular, the nanogranules cause a large S/V-ratio of skeletal carbonates and can thus promote effective oxygen isotope exchange with internal water at elevated temperatures. This is supported by the observations of Bernard et al. (2017), who observed extensive exchange with external water in foraminifera shells facilitated by their nanometer-scale granular structure. As a consequence, all biogenic carbonates, although heated under dry conditions, showed a decrease in $\delta^{18}O$ (this study; Henkes et al., 2014; Staudigel and Swart, 2016; Nooitgedacht et al., 2021), while this effect was smaller or not observed at all in abiogenic carbonates (this study, Passey and Henkes, 2012; Stolper and Eiler, 2015; Chen et al., 2019; Nooitgedacht et al., 2021). The internal water remains present in the biomineral during experimental heating, as shown by Nooitgedacht et al. (2021).

Our belemnite heating experiments show a simultaneous drop in $\delta^{18}O$ and Δ_{47} within the first 2–4 min of heating. The $\delta^{18}O$ remains unchanged afterwards (Fig. 3, Fig. S5d and Table S2), whereas Δ_{47} further decreases but at slower rates. This suggests that fast oxygen isotopes exchange between the mineral lattice and water at the crystal-water interface is the dominant control on clumped isotope resetting during initial heating of belemnite calcite. After oxygen-isotope equilibration with internal water, isotopic exchange between neighboring carbonate groups within the mineral lattice (i.e., solid-state bond reordering) becomes the dominant process on thermal resetting. In contrast, during heating of optical and spar calcites under wet conditions (Passey and Henkes, 2012; Brenner et al., 2018), the added water causes a slower, more gradual decrease in $\delta^{18}O$ over tens of hours of heating while resetting rates remain unaffected or are only moderately faster compared to dry conditions (Figure S5), which indicates that thermal resetting of these materials is dominated throughout the experiments by solid-state bond reordering. Furthermore, optical and spar calcites show no measurable change in $\delta^{18}O$ when heated under dry conditions, implying that they contain no significant amounts of internal water.

Accordingly, clumped isotope resetting in abiogenic carbonates with small S/V ratios is dominated by solid-state bond reordering, even when heated under wet conditions. Gradual shifts in calcite $\delta^{18}O$ during wet heating result from oxygen isotope exchange between the mineral and the water added at high water/rock ratios. However, mineral–water exchange is not efficient and does not substantially influence clumped isotope resetting rates. In contrast, clumped isotope resetting in biogenic carbonates with large S/V ratios is dominated by oxygen isotope exchange between the mineral lattice and internal water at low water/rock ratios within the first minutes of heating at experimental temperatures. Such oxygen isotope exchange may also continue after equilibration, but without further affecting $\delta^{18}O$ or Δ_{47}, and thermal resetting after equilibration is dominated by solid-state bond reordering.

Water fugacity as a key control on resetting rates of water-bearing skeletal carbonates can explain most experimental observations but not those for the WA-CB-13 Permian brachiopod calcite of Henkes et al. (2014). In that study, brachiopod kinetic parameters do not significantly differ from those of inorganic calcites (this study, Henkes et al., 2014; Stolper and Eiler, 2015; Hemingway and Henkes, 2021), even though the mechanism proposed here would predict resetting rates similar to belemnite calcite. The cause for the different behavior of the two materials remains an open question. EBSD data for the brachiopod WA-CB-11 (same location as WA-CB-13 used for the heating experiments in Henkes et al. (2014) and the study of Henkes et al. (2018); data provided by those authors) show good preservation of the primary textures and thus speak against recrystallization during burial (Fig. S15). Similarly, substantial pre-annealing of the brachiopod calcite seems unlikely, given the relatively high but still realistic initial Δ_{47} value corresponding to 31 °C. Instead, we suggest that differences in the amount and/or distribution of internal water might play a role.

4.4. Other potential factors influencing bond reordering rates in calcites

Oxygen isotope exchange with internal water initially present and/or expelled during heating by the thermal decomposition of organic compounds can explain rapid resetting of the belemnite calcite during the first minutes of experimental heating. However, even after full $\delta^{18}O$ equilibration with the internal water, the belemnite reordering rates are higher compared to all previously tested materials (Fig. S6). Thus, further material-specific properties must influence bond reordering rates.

4.4.1. Minor and trace element substitution

Minor and trace element substitutions influence crystallographic

defect concentrations in the mineral lattice and have been shown to promote oxygen self-diffusion in calcite (Kronenberg et al., 1984). Thus, they potentially influence bond reordering kinetics (Passey and Henkes, 2012; Henkes et al., 2014). The 32-times higher total concentration of calcium substitutions in the belemnite compared to our optical calcite (Table S3) agrees with the faster reordering of belemnite calcite. However, the relative proportions of different calcium substituting cations (Mg, Sr, Mn, Fe) may also play a role. According to the observed enrichments in belemnite calcite, Mg and Sr would thus be the most important cations influencing reordering rates. In the optical calcite, reordering would instead be dominated by Mg and Mn.

Minor and trace element data from other studies are also inconclusive. Passey and Henkes (2012) found that reordering kinetics in spar and optical calcite were similar despite spar containing 60 times more Mn. Furthermore, Henkes et al. (2014) found indistinguishable bond reordering kinetics between brachiopod and previously measured optical calcite (Passey and Henkes, 2012) despite the brachiopod containing 10 times more Mg. Stolper and Eiler (2015) interpreted these rate similarities as evidence that the observed fast reordering is caused by the higher initial concentration of pairs rather than trace element abundance. Further supporting this, Stolper and Eiler (2015) reported very similar bond reordering kinetics for their optical calcite, the optical

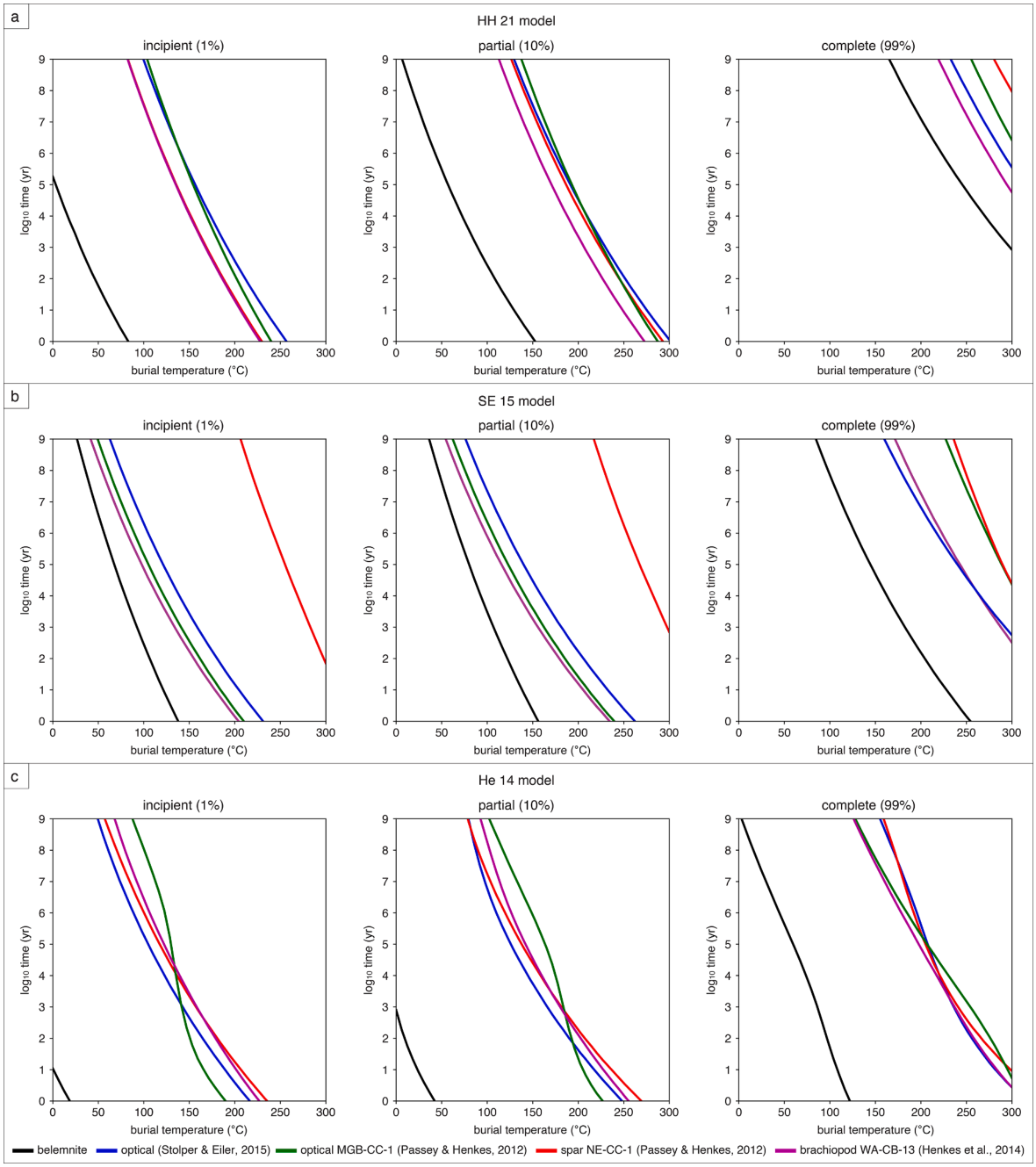

Fig. 6. Time-temperature fields for the preservation of Δ_{47} for different calcites predicted with the HH 21 (6a), SE 15 (6b), and He 14 (6c) models. To generate each line, the calcite with an initial Δ_{47} temperature of 20 °C is assumed to be instantaneously heated and held at a given temperature for a given amount of time. Colors indicate the different calcites. Note that incipient (1%) resetting is below the analytical error (e.g., below 1 °C change when heating a calcite with an initial Δ_{47} temperature of 20 °C to 200 °C). For predictions of MGB-CC-1 with the SE 15 model, we omitted the 475 °C experimental series as it yields unrealistically low activation energies (Fig. 11 in Stolper and Eiler (2015), re-shown here in Fig. S13a) and causes overestimation of the susceptibility of MGB-CC-1 to thermal resetting at geological timescales (i.e., faster resetting for optical calcite than belemnite; Figs. S13b and 13c).

calcite of Passey and Henkes (2012), and the brachiopod of Henkes et al. (2014), despite significant difference in Mg and Mn concentrations. Hemingway and Henkes (2021) similarly showed no statistically significant differences in bond reordering kinetics for the different materials tested previously when analyzed using the HH 21 model despite large differences in minor elemental compositions, which they interpreted as evidence for nearest-neighbor O–O distance as the primary control on reordering rates. Together, these observations speak against minor and trace element substitutions, particularly Mg and Mn, as being major controls on solid-state bond reordering rates.

4.4.2. Grain size

Carbonate groups on crystal boundaries are less energetically stable because they are bonded to fewer neighbors. Thus, such carbonate groups have lower activation energies for isotopic exchange, which results in higher susceptibility to solid-state bond reordering. We suggest that the large total area of crystal surfaces caused by the nano-granular structure of belemnite calcite contributes to the fast reordering. However, to fully equilibrate the clumped isotope composition, all carbonate groups within a nano-granule need to exchange. Calcite nanogranules typically show dimensions of tens of nanometers (Dauphin et al., 2018; Pérez-Huerta et al., 2018; Cuif et al., 2020), tenfold larger than the hexagonal unit-cell size of calcite (a = 5 Å, c = 17 Å). Large proportions of a nano-granule are thus not directly influenced by the less energetically stable grain surface. We therefore conclude that further factors control solid-state bond reordering rates, also after full equilibration with internal water.

4.5. Implications for thermal resetting of belemnite calcite at geological time scales

4.5.1. Model predictions

In the following, we discuss the implications of our belemnite experiments by investigating the differences in Δ_{47} evolution over geologic timescales between the belemnite and other calcites using the HH 21, SE 15, and He 14 reordering models. We explore three scenarios: (1) incipient resetting of 1% of the original signal, defining the time–temperature field for complete preservation of Δ_{47}; (2) partial resetting of 10%, corresponding to preservation of 90% of the difference between initial calcite Δ_{47} and that of equilibrium at the burial temperature; and (3) 99% resetting, defining the time–temperature field for complete Δ_{47} equilibration at the burial temperature. Importantly, the absolute temperature change resulting from a certain percentage of reordering increases with higher (burial) temperatures. Results are shown in Fig. 6.

The HH 21model predicts that the Δ_{47} of belemnite calcite begins to alter (1% resetting) after years to tens of years at 50–80 °C, whereas with the He 14 model, reordering starts even below 25 °C. However, 1% resetting for most applications is below the analytical error while 10 % is a more applicable measure for beginning Δ_{47} resetting that can be analytically resolved (Table 2).

The HH 21 and SE 15 models predict 10% resetting for burial during 100 kyr to 1 Myr at 40–60 °C (corresponding to an apparent temperature increase of 2–3 °C) and at 50–70 °C (corresponding to an apparent temperature increase of 3–4 °C), respectively. Notably, the He 14 model predicts 10% resetting in less than a year for the same range of burial temperatures.

Fig. 7 shows the evolution of the apparent Δ_{47} temperature predicted by the HH 21, SE 15, and He 14 models for belemnite calcite heated for 10^3-10^8 years at burial temperatures up to 200 °C. According to the HH 21 model, belemnite calcite with an initial Δ_{47} temperature of 20 °C experiencing moderate burial temperatures of 60–80 °C over tens of millions of years will reach apparent Δ_{47} temperatures of ~30–45 °C. Hot burial temperatures of 100–120 °C over the same timescale will lead to apparent Δ_{47} temperatures of ~65–90 °C, whereas for burial temperatures that never exceed 50 °C, the belemnite apparent Δ_{47} temperature will remain below 26 °C. For the SE 15 model, the belemnite apparent Δ_{47} temperature will increase to 30–50 °C if held at 60–80 °C and will fully equilibrate with ambient burial temperatures if held at 100–120 °C for tens of millions of years. If burial temperatures never exceed 50 °C, the belemnite apparent temperature will remain below 23 °C. In contrast to the HH 21 and SE 15 models, the He 14 model predicts full equilibration with any burial temperature above 20 °C for the timescale of tens of millions of years.

4.5.2. Empirical evaluation

To test if the belemnite calcite kinetic parameters are in agreement with real geological systems, we compare predicted vs. measured reordering for a specific field example using the HH 21, SE 15, and He 14 models. This test also implicitly assesses the ability of the three reordering models to additionally incorporate resetting by isotopic exchange with water, as all models were developed only considering solid-state bond reordering. We selected the Δ_{47} dataset of partially reordered Toarcian belemnites from Wutach, SW Germany, of Fernandez et al. (2021) because of the well-constrained regional burial history (Mazurek et al., 2006; Looser, 2022). The calculated Δ_{47} temperatures of individual belemnites range from 30 ± 8 to 54 ± 12 °C (95% CI) with an average of 41 ± 6 °C (Fernandez et al., 2021). The estimated range of original calcification temperatures is 23–33 °C, as calculated from the average $\delta^{18}O$ of the belemnites and assuming seawater $\delta^{18}O$ values of −1 to 1 ‰ (VSMOW). The calcification temperatures are calculated with the calcite-water oxygen isotope fractionation equation of Daëron et al. (2019), as it was shown by Vickers et al. (2021) that belemnites precipitate calcite close to oxygen isotope equilibrium.

The burial history is based on Mazurek et al. (2006), who used combined apatite fission track, vitrinite reflectance, and maturation-dependent biomarker data from the Benken deep borehole ~25 km

Table 2

Δ_{47} compositions and apparent temperatures of a calcite with an initial Δ_{47} corresponding to 20 °C that is heated at different burial temperatures and experiences 1, 10, 25, 75, and 99% resetting. For instance, when experiencing 10% resetting at 100 °C, the apparent Δ_{47} temperature of the calcite rises from 20 to 26 °C (corresponding to a drop in Δ_{47} from 0.609 to 0.592 ‰).

Burial temperature (°C)			40	60	80	100	120	140	160	180	200
$\Delta_{47,\ equilibrium}$ (‰ I-CDES)			0.553	0.506	0.468	0.435	0.407	0.383	0.362	0.344	0.329
Resetting of calcite with	1% reset.	$\Delta_{47,\ 1\%}$	0.608	0.608	0.608	0.607	0.607	0.607	0.607	0.606	0.606
$\Delta_{47,\ initial}$ = 0.609 ‰ corresponding to 20 °C		T $\Delta_{47,\ 1\%}$	20.2	20.3	20.5	20.6	20.6	20.7	20.8	20.9	20.9
	10% reset.	$\Delta_{47,\ 10\%}$	0.603	0.599	0.595	0.592	0.589	0.586	0.584	0.583	0.581
		T $\Delta_{47,\ 10\%}$	22	23	25	26	27	28	28	29	29
	25% reset.	$\Delta_{47,\ 25\%}$	0.595	0.583	0.574	0.566	0.559	0.553	0.547	0.543	0.539
		T $\Delta_{47,\ 25\%}$	25	29	32	35	38	40	42	44	46
	50% reset.	$\Delta_{47,\ 50\%}$	0.581	0.558	0.539	0.522	0.508	0.496	0.486	0.477	0.469
		T $\Delta_{47,\ 50\%}$	29	38	46	53	59	65	70	75	79
	75% reset.	$\Delta_{47,\ 75\%}$	0.567	0.532	0.503	0.479	0.458	0.440	0.424	0.410	0.399
		T $\Delta_{47,\ 75\%}$	35	49	61	74	86	97	108	117	126
	99% reset.	$\Delta_{47,\ 99\%}$	0.554	0.507	0.469	0.437	0.409	0.385	0.364	0.347	0.332
		T $\Delta_{47,\ 99\%}$	40	60	79	99	119	138	158	178	196

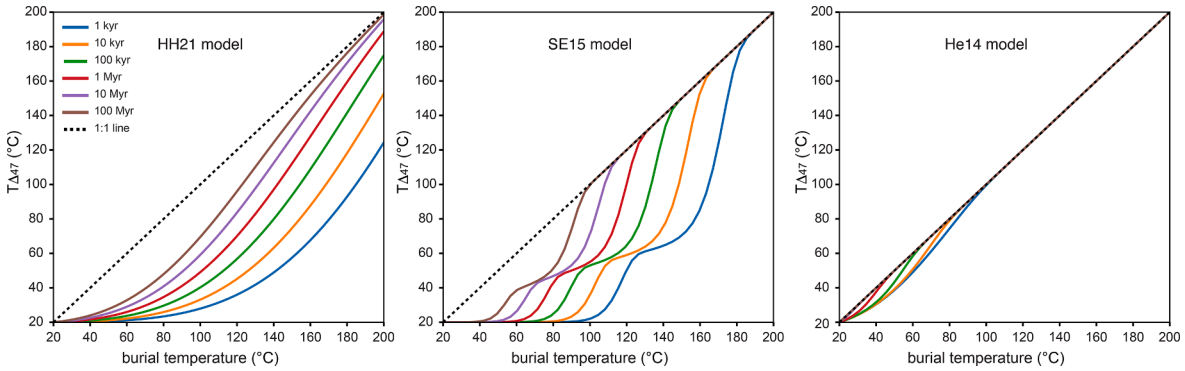

Fig. 7. Predictions for the evolution of the apparent Δ_{47} temperature of belemnite calcite initially at 20 °C that is heated instantaneously to the burial temperature and held for different amounts of time. Temperatures are calculated using the Anderson et al. (2021) calibration.

southeast of the study area. The burial history is further constrained by coupled Δ_{47} and U-Pb ages of vein carbonates in Early Jurassic sediments from Frick, ~50 km to the south-west (Looser, 2022). Combining both studies, we derived three possible scenarios for the burial history of Toarcian sediments in the Wutach area: in the (i) "no hyperthermalism" scenario (Fig. 8a,b), one episode of deep burial with a mean temperature of 91 ± 4 °C took place during the Early Cretaceous. Such temperatures were reached in the lower Jurassic as shown by a calcite cement with Δ_{47} temperatures of 97 ± 10 °C in Sinemurian sediments (Fernandez et al., 2021). In the (ii) "1 Ma hyperthermalism" and (iii) "16 Ma hyperthermalism" scenarios (Fig. 8c,d and 8e,f), both compatible with the U-Pb data of Looser (2022), an additional phase of hyperthermalism with temperatures of 117 ± 3 °C occurred between the Late Jurassic and the Early Cretaceous. This hyperthermal phase was observed for the Frick site but it is not documented for the Wutach area and thus should be regarded as maximal scenario. The same applies to burial temperatures of up to 66 °C suggested by Mazurek et al. (2006) during Oligocene to Miocene subsidence of the North Alpine Foreland Basin, as the Wutach area is located in a more marginal position in the basin than Benken and thus experienced less burial.

The evolution of apparent belemnite Δ_{47} temperature during burial (Fig. 8) is predicted with the kinetic parameters of the belemnite calcite and of the MGB-CC-1 optical calcite of Passey and Henkes (2012) for the He 14 and HH 21 models and the Mexico optical calcite of Stolper and Eiler (2015) for the SE 15 model. We chose the MGB-CC-1 optical calcite for the He 14 and HH 21 models because it has a more extensive dataset

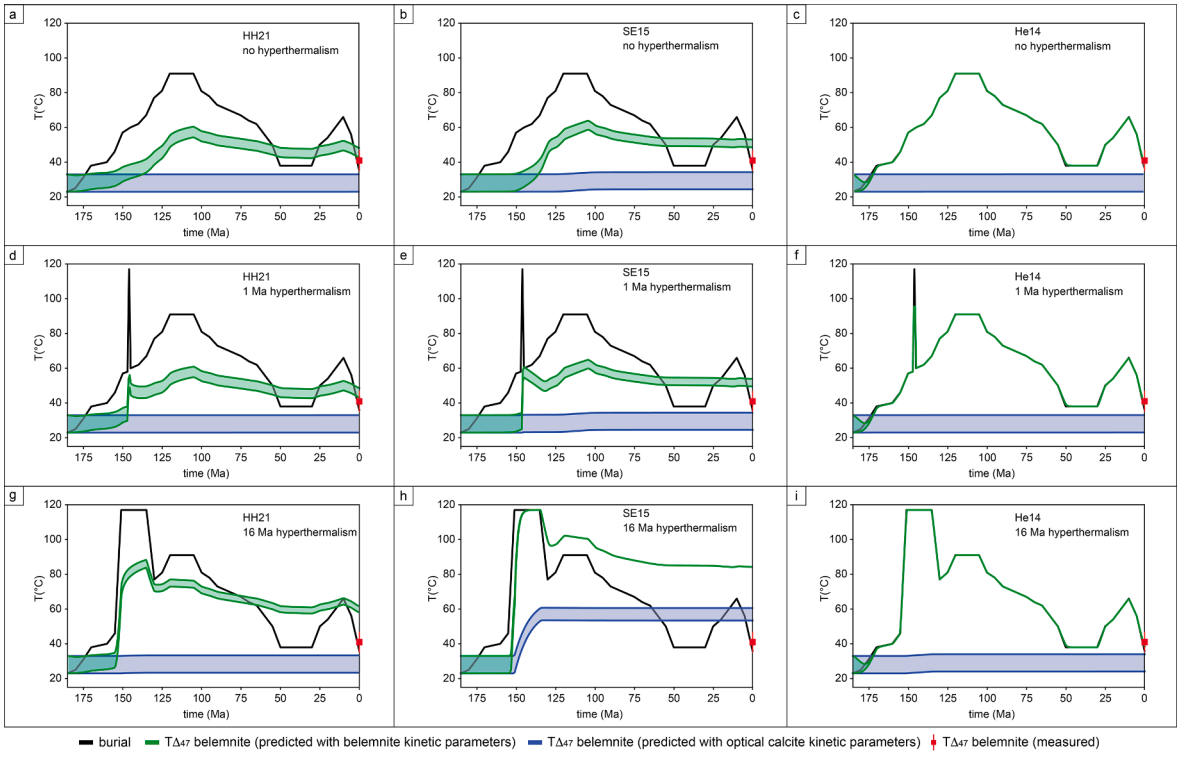

Fig. 8. Predicted change in calcite apparent Δ_{47} temperatures resulting from the experienced burial history (black). The evolution of apparent Δ_{47} temperatures is predicted with the HH 21 (a, d, g), the SE 15 (b, e, h), and the He 14 (c, f, i) reordering models using the kinetic parameters from the belemnite calcite of this study (green) and from optical calcites (blue). MGB-CC-1 optical calcite kinetic parameters are used for the HH 21 and He 14 models and Mexico optical calcite kinetic parameters for the SE 15 model. Precipitation of the belemnite calcite takes place at 185 Ma during Toarcian times with subsequent burial until today. The average Δ_{47} temperature of the belemnite calcite from Fernandez et al. (2021) is indicated with red squares on the right side of each diagram. Initial temperature of the belemnite calcite is in the range of 23 and 33 °C as constrained by the average belemnite $\delta^{18}O$ (VPDB) value and seawater values of −1 to 1 ‰ (Fernandez et al., 2021). Different burial scenarios are shown in the top (no hyperthermalism), middle (1 Ma hyperthermalism), and bottom (16 Ma hyperthermalism) rows.

from heating experiments than the Mexico calcite. For the SE 15 model, however, MGB-CC-1 predicts an unrealistically high susceptibility to thermal resetting at geological timescales (i.e., faster resetting than for belemnite; Fig. S13). Instead, using the SE 15 model with the Mexico optical calcite produces results in agreement with the other model predictions using either MGB-CC-1 or Mexico calcite kinetic parameters.

In summary, the three models consistently predict significantly higher apparent Δ_{47} temperatures when using the kinetic parameters of the belemnite compared to those of the optical calcite. Still, large differences in the predicted evolution of apparent belemnite Δ_{47} temperatures persist between the models. With the kinetic parameters of the MGB-CC-1 optical calcite, no significant resetting is predicted by the HH 21 and He 14 models for all burial scenarios (Fig. 8a,c,d,f,g,i). This is incompatible with the measured Δ_{47} of the belemnites showing an increase in apparent Δ_{47} temperatures in the range of 8 to 18 °C (from 23–33 °C to 41 ± 6 °C). Similarly, the SE 15 model with the Mexico optical calcite kinetic parameters for the "no hyperthermalism" and the "1 Ma hyperthermalism" scenarios predicts no significant resetting (Fig. 8b,e). For the "16 Ma hyperthermalism" scenario, however, the belemnite temperatures are clearly overestimated with apparent temperatures of 54–61 °C (Fig. 8h).

With the belemnite kinetic parameters, the HH 21 model predicts apparent temperatures of 43–48 °C for the "no hyperthermalism" (Fig. 8a) and 43–49 °C for the "1 Ma hyperthermalism" scenario (Fig. 8d), both in the range of the observed belemnite temperatures. For the "16 Ma hyperthermalism" scenario (Fig. 8g), the model yields clearly overestimated apparent temperatures of 58–62 °C. Compared to the HH 21 model, the SE 15 model predicts higher belemnite temperatures of 48–53 °C, 50–54 °C, and even 84 °C for the three scenarios (Fig. 8b,e,g). Notably, for the "16 Ma hyperthermalism" scenario, the SE 15 model predicts identical apparent Δ_{47} temperatures for belemnites, independently of their initial temperatures which range between 23 and 33 °C. In other words, thermal resetting would completely erase any initial temperature differences between individual belemnites. This is inconsistent with the observed temperature shift of 13 ± 4 °C across the Early Toarcian (Fernandez et al., 2021). The He 14 model in all scenarios is similarly incompatible with measured data since it predicts complete equilibration for burial temperatures as low as ~40 °C and thus complete homogenization of any initial temperature differences between samples (Fig. 8c,f,i).

Overall, by comparing model predictions using our belemnite kinetic parameters with field data, we show that the He 14 model does not accurately predict belemnite calcite resetting over geologic timescales, regardless of the burial scenario used. For the HH 21 and SE 15 models, predictions and measured belemnite temperatures for the two colder burial scenarios agree, showing that our belemnite reordering kinetic parameters provide realistic temperature predictions on geologic timescales. Finally, predicted temperatures for the HH 21 and the SE 15 models are between 15 and 35 °C higher when using the belemnite kinetic parameters instead of optical calcite. Using the kinetic parameters of optical calcite thus results in underestimation of the clumped isotope resetting of belemnites on geologic timescales.

The striking feature of the temperature predictions using belemnite kinetic parameters is the (partial) equilibration of belemnite Δ_{47} with burial temperatures as low ~40 °C for the HH 21 and ~55 °C for the SE 15 models. For a burial history including a sequence of deep burial and subsequent exhumation, this results in a strong dependence of the apparent belemnite Δ_{47} temperature on the cooling rates during exhumation. Similar to the cooling of carbonatites and marbles, apparent equilibrium Δ_{47} temperatures for belemnite calcite are colder for slower cooling rates (assuming the temperature at which thermal resetting beings was surpassed). Such re-equilibration during exhumation – which we term "retrograde resetting" – may overprint high Δ_{47} temperatures gained during preceding deep burial and result in an underestimation of the resetting experienced during geological history.

5. Conclusions

Our experimental data show faster clumped isotope resetting of belemnite rostral calcite compared to optical, spar, and brachiopod calcites. We propose that thermal resetting of belemnite calcite at higher rates and at lower ambient temperatures than inferred for other calcite materials is promoted by oxygen isotope exchange with trapped internal water. The ratio between the surface area of the crystal-water interface and the total crystal volume (S/V) is most likely the key control on reordering rates in water-bearing carbonate materials, as suggested in previous studies. For skeletal carbonates, the distinct micro- and nanostructures with hydrated inter- and intracrystalline organic matter result in a high S/V-ratio which allows oxygen isotope exchange with internal water becoming the dominant clumped isotope resetting mechanism on the total volume of the crystal. Accordingly, for skeletal carbonates, the first stage of rapid Δ_{47} resetting is dominated by oxygen isotope exchange with internal water at temperatures below those required for solid-state bond reordering. In the second stage, after calcite and internal water have equilibrated, isotopic exchange between neighboring carbonate groups within the mineral lattice (i.e., solid-state bond reordering) becomes the dominant resetting mechanism. In contrast to skeletal carbonates, thermal resetting in optical calcite is dominated by solid-state bond reordering throughout. Continued faster Δ_{47} reordering of belemnite compared to optical calcite after equilibration with internal water suggest that further material-specific properties influence solid-state bond reordering rates. On an atomic scale, calcites may or may not share common resetting kinetics, and it remains unclear to what extent lattice defects influence reordering rates. However, at a larger scale, calcite materials differ by their potential to interact with water and further material-specific properties that result in differences in resetting kinetics and the susceptibility to clumped isotope reordering among calcites. Our experiments demonstrate the need for material-specific clumped isotope resetting kinetics, especially for skeletal carbonates. Working with kinetic parameters derived for materials that are very different from the application may result in erroneous temperature reconstructions. Ultimately, our belemnite-specific kinetic parameters allow for more accurate paleotemperature estimations using partially reset belemnites.

Author contribution

NL, AF, and SMB designed the study. NL prepared the samples, conducted the clumped isotope measurements, and wrote the manuscript with contributions from all co-authors. PP conducted the heating experiments, performed the XRD analyses, and determined the stable isotope composition of the added CO_2. JDH derived the Arrhenius kinetic parameters and carried out the calculations on clumped isotope resetting at geological time scales. APH and LGM carried out the EBSD analyses and data interpretation. MLV and GDP provided the belemnite rostrum.

Declaration of Competing Interest

The authors declare that they have no known competing financial interests or personal relationships that could have appeared to influence the work reported in this paper.

Acknowledgments

This study was funded by the Swiss National Science Foundation project number 200021_169849. Funding to AF from Juan de la Cierva Fellowship (IJC2019040065-I) granted by the Spanish Ministry of Science and Innovation and co-funded by the European Development Fund and the European Social Fund. Funding to MLV from the European Commission, Horizon 2020 (ICECAP; grant no. 101024218), and the Research Council of Norway Centre of Excellence funding scheme,

project number 223272. EBSD data for the WA-CB-11 brachiopod provided by the authors of Henkes et al. (2014) was obtained with support from the US National Science Foundation (EAR-1226832). We thank Ethan Grossman and an anonymous reviewer for their helpful comments, and Weifu Guo for his comments and careful handling of the manuscript.

Appendix A. Supplementary material

Contents of the supplementary files include stable and clumped isotope data (both data table and raw data), trace elemental data, XRD data, EBSD data of WA-CB-11 brachiopod, additional figures of the evolution of $\delta^{18}O$ and Δ_{47} compositions for different calcite materials, and model fits of the optical and belemnite calcites for the HH 21, SE 15, and He 14 models. Supplementary data to this article can be found online at https://doi.org/10.1016/j.gca.2023.03.030.

References

Anderson, N.T., Kelson, J.R., Kele, S., Daëron, M., Bonifacie, M., Horita, J., Mackey, T.J., John, C.M., Kluge, T., Petschnig, P., Jost, A.B., Huntington, K.W., Bernasconi, S.M., Bergmann, K.D., 2021. A Unified Clumped Isotope Thermometer Calibration (0.5–1,100°C) Using Carbonate-Based Standardization. Geophys. Res. Lett. 48, 1–11.

Bajnai, D., Guo, W., Spötl, C., Coplen, T.B., Methner, K., Löffler, N., Krsnik, E., Gischler, E., Hansen, M., Henkel, D., Price, G.D., Raddatz, J., Scholz, D., Fiebig, J., 2020. Dual clumped isotope thermometry resolves kinetic biases in carbonate formation temperatures. Nat. Commun. 11, 1–9.

Bernard, S., Daval, D., Ackerer, P., Pont, S., Meibom, A., 2017. Burial-induced oxygen-isotope re-equilibration of fossil foraminifera explains ocean paleotemperature paradoxes. Nat. Commun. 8, 1–10.

Bernasconi, S.M., Hu, B., Wacker, U., Fiebig, J., Breitenbach, S.F.M., Rutz, T., 2013. Background effects on Faraday collectors in gas-source mass spectrometry and implications for clumped isotope measurements. Rapid Commun. Mass Spectrom. 27, 603–612.

Bernasconi, S.M., Müller, I.A., Bergmann, K.D., Breitenbach, S.F.M., Fernandez, A., Hodell, D.A., Jaggi, M., Meckler, A.N., Millan, I., Ziegler, M., 2018. Reducing uncertainties in carbonate clumped isotope analysis through consistent carbonate-based standardization. Geochem. Geophys. Geosystems 19, 2895–2914.

Bernasconi, S.M., Daëron, M., Bergmann, K.D., Bonifacie, M., Meckler, A.N., Affek, H.P., Anderson, N., Bajnai, D., Barkan, E., Beverly, E., Blamart, D., Burgener, L., Calmels, D., Chaduteau, C., Clog, M., Davidheiser-Kroll, B., Davies, A., Dux, F., Eiler, J., Elliott, B., Fetrow, A.C., Fiebig, J., Goldberg, S., Hermoso, M., Huntington, K.W., Hyland, E., Ingalls, M., Jaggi, M., John, C.M., Jost, A.B., Katz, S., Kelson, J., Kluge, T., Kocken, I.J., Laskar, A., Leutert, T.J., Liang, D., Lucarelli, J., Mackey, T.J., Mangenot, X., Meinicke, N., Modestou, S.E., Müller, I.A., Murray, S., Neary, A., Packard, N., Passey, B.H., Pelletier, E., Petersen, S., Piasecki, A., Schauer, A., Snell, K.E., Swart, P.K., Tripati, A., Upadhyay, D., Vennemann, T., Winkelstern, I., Yarian, D., Yoshida, N., Zhang, N., Ziegler, M., 2021. InterCarb: A Community Effort to Improve Interlaboratory Standardization of the Carbonate Clumped Isotope Thermometer Using Carbonate Standards. Geochemistry. Geophys. Geosystems 22, 1–25.

Brenner, D.C., Passey, B.H., Stolper, D.A., 2018. Influence of water on clumped-isotope bond reordering kinetics in calcite. Geochim. Cosmochim. Acta 224, 42–63.

Brenner, D.C., Passey, B.H., Holder, R.M., Viete, D.R., 2021. Clumped-Isotope Geothermometry and Carbonate U-Pb Geochronology of the Alta Stock Metamorphic Aureole, Utah, USA: Insights on the Kinetics of Metamorphism in Carbonates. Geochem. Geophys. Geosystems 22, 1–21.

Came, R.E., Eiler, J.M., Veizer, J., Azmy, K., Brand, U., Weidman, C.R., 2007. Coupling of surface temperatures and atmospheric CO_2 concentrations during the Palaeozoic era. Nature 449, 5–9.

Chen, S., Ryb, U., Piasecki, A.M., Lloyd, M.K., Baker, M.B., Eiler, J.M., 2019. Mechanism of solid-state clumped isotope reordering in carbonate minerals from aragonite heating experiments. Geochim. Cosmochim. Acta 258, 156–173.

Cuif, J.P., Dauphin, Y., Berthet, P., Jegoudez, J., 2004. Associated water and organic compounds in coral skeletons: Quantitative thermogravimetry coupled to infrared absorption spectrometry. Geochem. Geophys. Geosystems 5, 1–9.

Cuif, J.P., Belhadj, O., Borensztajn, S., Gèze, M., Trigos-Santos, S., Prado, P., Dauphin, Y., 2020. Prism substructures in the shell of Pinna nobilis (Linnaeus, 1758), Mollusca – Evidence for a three-dimensional pulsed-growth model. Heliyon 6.

Daëron, M., Drysdale, R.N., Peral, M., Huyghe, D., Blamart, D., Coplen, T.B., Lartaud, F., Zanchetta, G., 2019. Most Earth-surface calcites precipitate out of isotopic equilibrium. Nat. Commun. 10, 1–7.

Dauphin, Y., Luquet, G., Perez-Huerta, A., Salomé, M., 2018. Biomineralization in modern avian calcified eggshells: similarity versus diversity. Connect. Tissue Res. 59, 67–73.

Davies, A.J., John, C.M., 2017. Reducing contamination parameters for clumped isotope analysis: The effect of lowering PorapakTM Q trap temperature to below –50°C. Rapid Commun. Mass Spectrom. 31, 1313–1323.

Dennis, K.J., Schrag, D.P., 2010. Clumped isotope thermometry of carbonatites as an indicator of diagenetic alteration. Geochim. Cosmochim. Acta 74, 4110–4122.

Eiler, J.M., 2011. Paleoclimate reconstruction using carbonate clumped isotope thermometry. Quat. Sci. Rev. 30, 3575–3588.

Farver, J.R., 1994. Oxygen self-diffusion in calcite: Dependence on temperature and water fugacity and water fugacity. Earth Planet. Sci. Lett. 121, 575–587.

Fernandez, A., Müller, I.A., Rodríguez-Sanz, L., van Dijk, J., Looser, N., Bernasconi, S.M., 2017. A Reassessment of the Precision of Carbonate Clumped Isotope Measurements: Implications for Calibrations and Paleoclimate Reconstructions. Geochem. Geophys. Geosystems 18, 4375–4386.

Fernandez, A., Korte, C., Ullmann, C.V., Looser, N., Wohlwend, S., Bernasconi, S.M., 2021. Reconstructing the magnitude of Early Toarcian (Jurassic) warming using the reordered clumped isotope compositions of belemnites. Geochim. Cosmochim. Acta 293, 308–327.

Gaffey, S.J., 1988. Water in skeletal carbonates. J. Sediment. Petrol. 58, 397–414.

Ghosh, P., Adkins, J., Affek, H., Balta, B., Guo, W., Schauble, E.A., Schrag, D., Eiler, J.M., 2006. ^{13}C–^{18}O bonds in carbonate minerals: A new kind of paleothermometer. Geochim. Cosmochim. Acta 70, 1439–1456.

Glass, K., Ito, S., Wilby, P.R., Sota, T., Nakamura, A., Russell Bowers, C., Miller, K.E., Dutta, S., Summons, R.E., Briggs, D.E.G., Wakamatsu, K., Simon, J.D., 2013. Impact of diagenesis and maturation on the survival of eumelanin in the fossil record. Org. Geochem. 64, 29–37.

Green, P.F., Thomson, K., Hudson, J.D., 2001. Recognition of tectonic events in undeformed regions: Contrasting results from the Midland Platform and East Midlands Shelf, Central England. J. Geol. Soc. London. 158, 59–73.

Hemingway, J.D., Henkes, G.A., 2021. A disordered kinetic model for clumped isotope bond reordering in carbonates. Earth Planet. Sci. Lett. 566, 116962.

Hemingway, J.D., 2020. Isotopylog: Open-source tools for clumped isotope kinetic data analysis.

Henkes, G.A., Passey, B.H., Grossman, E.L., Shenton, B.J., Pérez-Huerta, A., Yancey, T.E., 2014. Temperature limits for preservation of primary calcite clumped isotope paleotemperatures. Geochim. Cosmochim. Acta 139, 362–382.

Henkes, G.A., Passey, B.H., Grossman, E.L., Shenton, B.J., Yancey, T.E., Pérez-Huerta, A., 2018. Temperature evolution and the oxygen isotope composition of Phanerozoic oceans from carbonate clumped isotope thermometry. Earth Planet. Sci. Lett. 490, 40–50.

Hoffmann, R., Stevens, K., 2020. The palaeobiology of belemnites – foundation for the interpretation of rostrum geochemistry. Biol. Rev. 95, 94–123.

Hudson, J.D., Martill, D.M., 1994. The Peterborough Member (Callovian, Middle Jurassic) of the Oxford Clay Formation at Peterborough, UK. J. Geol. Soc. London. 151, 113–124.

Huntington, K.W., Lechler, A.R., 2015. Carbonate clumped isotope thermometry in continental tectonics. Tectonophysics 647, 1–20.

John, C.M., Bowen, D., 2016. Community software for challenging isotope analysis : First applications of 'Easotope' to clumped isotopes. Rapid Commun. Mass Spectrom. 2285–2300.

Kenig, F., Hudson, J.D., Damsté, J.S.S., Popp, B.N., 2004. Intermittent euxinia: Reconciliation of a Jurassic black shale with its biofacies. Geology 32, 421–424.

Kronenberg, A.K., Yund, R.A., Giletti, B.J., 1984. Carbon and oxygen diffusion in calcite: Effects of Mn content and P_{H2O}. Phys. Chem. Miner. 11, 101–112.

Labotka, T.C., Cole, D.R., Fayek, M.J., Chacko, T., 2011. An experimental study of the diffusion of C and O in calcite in mixed CO_2-H_2O fluid. Am. Mineral. 96, 1262–1269.

Lawson, M., Shenton, B.J., Stolper, D.A., Eiler, J.M., Rasbury, E.T., Becker, T.P., Phillips-Lander, C.M., Buono, A.S., Becker, S.P., Pottorf, R., Gray, G.G., Yurewicz, D., Gournay, J., 2018. Deciphering the diagenetic history of the El Abra Formation of eastern Mexico using reordered clumped isotope temperatures and U-Pb dating. Bull. Geol. Soc. Am. 130, 617–629.

Li, Q., McArthur, J.M., Doyle, P., Janssen, N., Leng, M.J., Müller, W., Reboulet, S., 2013. Evaluating Mg/Ca in belemnite calcite as a palaeo-proxy. Palaeogeogr. Palaeoclimatol. Palaeoecol. 388, 98–108.

Lloyd, M.K., Eiler, J.M., Nabelek, P.I., 2017. ScienceDirect Clumped isotope thermometry of calcite and dolomite in a contact metamorphic environment. Geochim. Cosmochim. Acta 197, 323–344.

Lloyd, M.K., Ryb, U., Eiler, J.M., 2018. Experimental calibration of clumped isotope reordering in dolomite. Geochim. Cosmochim. Acta 242, 1–20.

Looser, N., Madritsch, H., Guillong, M., Laurent, O., Wohlwend, S., Bernasconi, S.M., 2021. Absolute Age and Temperature Constraints on Deformation Along the Basal Décollement of the Jura Fold-and-Thrust Belt From Carbonate U-Pb Dating and Clumped Isotopes. Tectonics 40, 1–16.

Looser, N.S.H., 2022. Coupling Clumped Isotope Thermometry and U-Pb Dating of Carbonates for Applications in Stratigraphy, Diagenesis, and Geodyamics. Diss. ETH No. 28365. ETH Zurich.

Loyd, S.J., Dickson, J.A.D., Boles, J.R., Tripati, A.K., 2014. Clumped-isotope constraints on cement paragenesis in septarian concretions. J. Sediment. Res. 84, 1170–1184.

Marland, G., 1975. The stability of $CaCO_3 \cdot 6H_2O$ (ikaite). Geochim. Cosmochim. Acta 39, 83–91.

Mazurek, M., Hurford, A.J., Leu, W., 2006. Unravelling the multi-stage burial history of the Swiss Molasse Basin: Integration of apatite fission track, vitrinite reflectance and biomarker isomerisation analysis. Basin Res. 18, 27–50.

Meckler, A.N., Ziegler, M., Millán, M.I., Breitenbach, S.F.M., Bernasconi, S.M., 2014. Long-term performance of the Kiel carbonate device with a new correction scheme for clumped isotope measurements. Rapid Commun. Mass Spectrom. 28, 1705–1715.

Millán, M.I., Machel, H., Bernasconi, S.M., 2016. Constraining Temperatures of Formation and Composition of Dolomitizing Fluids In the Upper Devonian Nisku Formation (Alberta, Canada) With Clumped Isotopes. J. Sediment. Res. 86, 107–112.

Müller, I.A., Fernandez, A., Radke, J., van Dijk, J., Bowen, D., Schwieters, J., Bernasconi, S.M., 2017. Carbonate clumped isotope analyses with the long-

integration dual-inlet (LIDI) workflow: scratching at the lower sample weight boundaries. Rapid Commun. Mass Spectrom. 31, 1057–1066.
Mutterlose, J., Malkoc, M., Schouten, S., Sinninghe Damsté, J.S., Forster, A., 2010. TEX_{86} and stable $\delta^{18}O$ paleothermometry of early Cretaceous sediments: Implications for belemnite ecology and paleotemperature proxy application. Earth Planet. Sci. Lett. 298, 286–298.
Nooitgedacht, C.W., van der Lubbe, H.J.L., Ziegler, M., Staudigel, P.T., 2021. Internal Water Facilitates Thermal Resetting of Clumped Isotopes in Biogenic Aragonite. Geochem. Geophys. Geosystems 22, 1–13.
Passey, B.H., Henkes, G.A., 2012. Carbonate clumped isotope bond reordering and geospeedometry. Earth Planet. Sci. Lett. 351–352, 223–236.
Passey, B.H., Hu, H., Ji, H., Montanari, S., Li, S., Henkes, G.A., Levin, N.E., 2014. ScienceDirect Triple oxygen isotopes in biogenic and sedimentary carbonates. Geochim. Cosmochim. Acta 141, 1–25.
Pérez-Huerta, A., Cusack, M., England, J., 2007. Crystallography and diagenesis in fossil craniid brachiopods. Palaeontology 50, 757–763.
Pérez-Huerta, A., Coronado, I., Hegna, T.A., 2018. Understanding biomineralization in the fossil record. Earth-Sci. Rev. 179, 95–122.
Price, G.D., Passey, B.H., Berriasian, S.C., 2013. Dynamic polar climates in a greenhouse world: Evidence from clumped isotope thermometry of Early Cretaceous belemnites. Geology 41, 923–926.
Price, G.D., Hart, M.B., Wilby, P.R., Page, K.N., 2015. Isotopic analysis of Jurassic (Callovian) mollusks from the christian malford lagerstätte (UK): Implications for ocean water temperature estimates based on belemnoids. Palaios 30, 645–654.
Ritter, A.C., Mavromatis, V., Dietzel, M., Kwiecien, O., Wiethoff, F., Griesshaber, E., Casella, L.A., Schmahl, W.W., Koelen, J., Neuser, R.D., Leis, A., Buhl, D., Niedermayr, A., Breitenbach, S.F.M., Bernasconi, S.M., Immenhauser, A., 2017. Exploring the impact of diagenesis on (isotope) geochemical and microstructural alteration features in biogenic aragonite. Sedimentology 64, 1354–1380.
Ryb, U., Lloyd, M.K., Stolper, D.A., Eiler, J.M., 2017. The clumped-isotope geochemistry of exhumed marbles from Naxos, Greece. Earth Planet. Sci. Lett. 470, 1–12.
Ryb, U., Lloyd, M.K., Eiler, J.M., 2021. Carbonate clumped isotope constraints on burial, uplift and exhumation histories of the Colorado Plateau. Earth Planet. Sci. Lett. 566, 116964.
Schauble, E.A., Ghosh, P., Eiler, J.M., 2006. Preferential formation of ^{13}C–^{18}O bonds in carbonate minerals, estimated using first-principles lattice dynamics. Geochim. Cosmochim. Acta 70, 2510–2529.
Scheele, N., Hoefs, J., 1992. Carbon isotope fractionation between calcite, graphite and CO_2: an experimental study. Contrib. to Mineral. Petrol. 112, 35–45.
Schmid, T.W., Bernasconi, S.M., 2010. An automated method for ‘ clumped-isotope ’ measurements on small carbonate samples, 1955–1963.
Shenton, B.J., Grossman, E.L., Passey, B.H., Henkes, G.A., Becker, T.P., Laya, J.C., Perez-Huerta, A., Becker, S.P., Lawson, M., 2015. Clumped isotope thermometry in deeply buried sedimentary carbonates: The effects of bond reordering and recrystallization. Bull. Geol. Soc. Am. 127, 1036–1051.
Staudigel, P.T., Swart, P.K., 2016. Isotopic behavior during the aragonite-calcite transition: Implications for sample preparation and proxy interpretation. Chem. Geol. 442, 130–138.
Stevens, K., Griesshaber, E., Schmahl, W., Casella, L.A., Iba, Y., Mutterlose, J., 2017. Belemnite biomineralization, development, and geochemistry: The complex rostrum of Neohibolites minimus. Palaeogeogr. Palaeoclimatol. Palaeoecol. 468, 388–402.
Stolper, D.A., Eiler, J.M., 2015. The kinetics of solid-state isotope-exchange reactions for clumped isotopes: A study of inorganic calcites and apatites from natural and experimental samples. Am. J. Sci. 315, 363–411.
Ullmann, C.V., Frei, R., Korte, C., Hesselbo, S.P., 2015. Chemical and isotopic architecture of the belemnite rostrum. Geochim. Cosmochim. Acta 159, 231–243.
Vickers, M.L., Fernandez, A., Hesselbo, S.P., Price, G.D., Bernasconi, S.M., Lode, S., Ullmann, C.V., Thibault, N., Hougaard, I.W., Korte, C., 2020. Unravelling Middle to Late Jurassic palaeoceanographic and palaeoclimatic signals in the Hebrides Basin using belemnite clumped isotope thermometry. Earth Planet. Sci. Lett. 546, 116401.
Vickers, M.L., Bernasconi, S.M., Ullmann, C.V., Lode, S., Looser, N., Morales Grafulha, L., Price, G.D., Wilby, P.R., Hougård, I.W., Hesselbo, S.P., Korte, C., 2021. Marine temperatures underestimated for past greenhouse climate. Sci. Rep. 1–9.
Voigt, S., Wilmsen, M., Mortimore, R.N., Voigt, T., 2003. Cenomanian palaeotemperatures derived from the oxygen isotopic composition of brachiopods and belemnites: Evaluation of Cretaceous palaeotemperature proxies. Int. J. Earth Sci. 92, 285–299.
Wang, Z., Schauble, E.A., Eiler, J.M., 2004. Equilibrium thermodynamics of multiply substituted isotopologues of molecular gases. Geochim. Cosmochim. Acta 68, 4779–4797.
Wilby, P.R., Duff, K., Page, K., Martin, S., 2008. Feature preserving the unpreservable: a lost world. Geol. Today 24, 95–98.